Towards the complete census of molecular hydrogen in a simulated disc galaxy

Nickerson, Sarah ; Teyssier, Romain ; Rosdahl, Joakim

Abstract: We present a multiscale analysis of molecular hydrogen in a Milky Way-like simulated galaxy. Our census covers the gas content of the entire disc, to radial profiles and the Kennicutt–Schmidt relation, to a study of its molecular clouds, and finally down to a cell-by-cell analysis of the gas phases. A significant fraction of the H2 gas is in low-density regions mixed with atomic hydrogen and would therefore be difficult to observe. We use the molecular addition to ramses-rt, an adaptive mesh refinement grid code with the hydrodynamics coupled to moment-based radiative transfer. Three resolutions of the same galaxy detail the effects it has on H2 formation, with grid cells sized 97, 24, and 6.1 pc. Only the highest resolution yields gas densities high enough to host significant H2 fractions, and resolution is therefore key to simulating H2. Our H2 content is not completely converged but we find general agreement with available observations. Apart our pieces of galactic analysis are disparate, but assembled, they provide a cohesive portrait of H2 in the interstellar medium. H2 chemistry on the atomic scale is sufficient to generate its dynamics throughout an entire galaxy.

DOI: https://doi.org/10.1093/mnras/stz048

Monthly Notices
of the
ROYAL ASTRONOMICAL SOCIETY

MNRAS **484,** 1238–1256 (2019)
Advance Access publication 2019 January 9

doi:10.1093/mnras/stz048

Towards the complete census of molecular hydrogen in a simulated disc galaxy

Sarah Nickerson [1]★ Romain Teyssier[1] and Joakim Rosdahl [2]

[1]*Institute for Computational Science, University of Zürich, Winterthurerstrasse 190, CH-8057 Zürich, Switzerland*
[2]*Centre for Astronomy Research, University of Lyon, 9 avenue Charles André, F-69230 Saint-Genis-Laval, France*

Accepted 2019 January 3. Received 2018 November 30; in original form 2018 September 4

ABSTRACT

We present a multiscale analysis of molecular hydrogen in a Milky Way-like simulated galaxy. Our census covers the gas content of the entire disc, to radial profiles and the Kennicutt–Schmidt relation, to a study of its molecular clouds, and finally down to a cell-by-cell analysis of the gas phases. A significant fraction of the H_2 gas is in low-density regions mixed with atomic hydrogen and would therefore be difficult to observe. We use the molecular addition to RAMSES-RT, an adaptive mesh refinement grid code with the hydrodynamics coupled to moment-based radiative transfer. Three resolutions of the same galaxy detail the effects it has on H_2 formation, with grid cells sized 97, 24, and 6.1 pc. Only the highest resolution yields gas densities high enough to host significant H_2 fractions, and resolution is therefore key to simulating H_2. Our H_2 content is not completely converged but we find general agreement with available observations. Apart our pieces of galactic analysis are disparate, but assembled, they provide a cohesive portrait of H_2 in the interstellar medium. H_2 chemistry on the atomic scale is sufficient to generate its dynamics throughout an entire galaxy.

Key words: molecular processes – radiative transfer – methods: numerical – galaxies: formation.

1 INTRODUCTION

Molecular hydrogen (H_2) is the most common molecule in the Universe (Herbst 2001). It is critical to cooling the interstellar medium (Glover & Abel 2008). Cold and dense giant molecular clouds (GMCs) are associated with young stars and star formation (Blaauw 1964; Werner et al. 1977; Blitz & Thaddeus 1980; Genzel & Stutzki 1989). Despite its importance, molecular hydrogen is challenging to detect directly through observations (Young & Scoville 1991). CO is a secondary tracer of dense gas and is easily observed. H_2 abundance is inferred by a conversion factor from CO abundance, conventionally taken as a constant for the Milky Way (Bolatto, Wolfire & Leroy 2013), and in external galaxies it varies mainly as a function of metallicity (Accurso et al. 2017). Modern observations are pushing forward the boundaries of our understanding of H_2 to increased precision and more distant galaxies. H_2 is measured extensively for the Milky Way, the Local Group, and galaxies beyond, on scales that range from total gas content, to radially resolved profiles, and to individual GMCs.

The Kennicutt–Schmidt (KS) relation links the star formation rate (SFR) surface density to the gas surface density by a power law. Schmidt (1959) infers this from analysis in the solar neighbourhood. Later, Kennicutt (1989) successfully applies this relation to the overall surface densities of external galaxies. New measurements that resolve the structure of external galaxies and the H_2 within them (Bigiel et al. 2008) find that the correlation is tighter between H_2 and SFR than total neutral hydrogen and SFR, as Leroy et al. (2013) confirm. The combined xCOLD GASS (Saintonge et al. 2017) CO and xGASS (Catinella et al. 2018) surveys of over 1000 galaxies find a weak correlation between the total molecular gas content and the SFR.

In an early study of Galactic GMCs, Larson (1981) derives a relation in which the cloud's velocity dispersion scales with its size. Solomon et al. (1987) refine this relation with a larger catalogue, and Heyer et al. (2009) challenge this relation to show that the velocity dispersion not only depends on the size but also the surface density of the molecular cloud. They argue that earlier surveys lacked proper spatial resolution and mistook cloud surface density to be constant. Rice et al. (2016) with data from Dame, Hartmann & Thaddeus (2001) study GMCs in all regions of the Galaxy to show that the Larson relation holds throughout the Galaxy, but that the inner Galaxy tends to have more massive clouds. Miville-Deschênes, Murray & Lee (2017) process these data differently and also provide a detailed analysis of cloud properties. New surveys (Rosolowsky 2007; Bolatto et al. 2008; Colombo et al. 2014; Leroy et al. 2017; Sun et al. 2018) create GMC catalogues beyond the Milky Way and discover a similar environment and relations, though Colombo et al.

★ E-mail: snickers@physik.uzh.ch

(2014) find the original Larson relation between velocity dispersion and cloud size to be weak.

The era of increasing precision for H_2 measurement requires a similar increase in sophistication for simulations. Several codes use an equilibrium model to define the H_2 content, under the assumption that the chemistry in each volume element is in an equilibrium state determined by purely local variables. The most common formulation, in use by Kuhlen et al. (2012), Halle & Combes (2013), Thompson et al. (2014), and Hopkins et al. (2014), is developed in Krumholz, McKee & Tumlinson (2008), Krumholz & Gnedin (2011), and McKee & Krumholz (2010) (hereafter KMT) where the H_2 fraction is calculated from postulating an H I–H_2 sphere in a homogeneous radiation field. Krumholz (2013) updates this model for the molecular-poor regime. The equilibrium model of Robertson & Kravtsov (2008) is based on the photoionization code CLOUDY (Ferland et al. 1998), and Pelupessy, Papadopoulos & Van Der Werf (2006) use a subgrid model of cloud populations.

Gnedin, Tassis & Kravtsov (2009) pioneer a non-equilibrium chemical network for H_2, employing rate equations to track locally atomic and molecular hydrogen in their galaxy simulations with the ART code (Kravtsov 1999). Gnedin & Kravtsov (2011) expand this network, introducing ionized hydrogen and helium species. Many chemical networks for nearly as many codes follow. Christensen et al. (2012) and Tomassetti et al. (2014) adapt this method for GASOLINE (Wadsley, Stadel & Quinn 2004) and RAMSES (Teyssier 2002), respectively. Baczynski, Glover & Klessen (2015) adapt the chemical network in Nelson & Langer (1997), Glover & Mac Low (2007a), Glover & Mac Low (2007b), and Glover & Clark (2012) for FLASH4 (Fryxell et al. 2000; Dubey, Reid & Fisher 2008); Richings & Schaye (2016) adapt the network in Richings, Schaye & Oppenheimer (2014a,b) for GADGET3 (Springel 2005); Hu et al. (2016) also adapt the Glover & Clark (2012) network but for GADGET3; and Katz et al. (2017) follow Baczynski et al. (2015)'s adaptation for RAMSES-RT (Rosdahl et al. 2013). Pallottini et al. (2017), Capelo et al. (2018), and Lupi et al. (2018) meld the KROME (Grassi et al. 2014) chemical network with RAMSES, GASOLINE2 (Wadsley, Keller & Quinn 2017), and GIZMO (Hopkins 2015), respectively.

A direct comparison between the KMT equilibrium model and non-equilibrium models shows that they diverge at low metallicities (Krumholz & Gnedin 2011), that the non-equilibrium models are capable of maintaining H_2 at lower densities (Tomassetti et al. 2014), and that the non-equilibrium models are clumpier and closer to the KS relation (Pallottini et al. 2017).

Non-equilibrium chemistry becomes even more powerful when coupled to the radiative transfer of the photons that dissociate and ionize the gas. Two radiative transfer methods are currently in use. Baczynski et al. (2015) employ ray tracing, which has the advantage of computing exact column densities. However, the computational cost of ray tracing is proportional to the number of radiation sources and this becomes less feasible in galaxy simulations filled with stars. Another option is to use a moment-based method in which the gas is treated as a fluid, and this is much more feasible for galaxy simulations. Gnedin & Kravtsov (2011), Lupi et al. (2018), and RAMSES-RT (Rosdahl et al. 2013) use this method.

Many of the chemical networks follow similar models for the formation and destruction of H_2, but two choices in how to model the subgrid physics differentiate them.

The first is whether to include a clumping factor, the purpose of which is to account for unresolved dense structure in molecular clouds. Practically, this amounts to enhancing H_2 formation by some factor. The most commonly used constant for the clumping factor (Christensen et al. 2012; Katz et al. 2017; Capelo et al. 2018) is 10 from Gnedin et al. (2009), who reason that this is the ratio of average H_2 density to cloud density (McKee & Ostriker 2007). Micic et al. (2012) find that a constant clumping factor may lead to an overprediction of H_2 in high-density regions. Capelo et al. (2018) compare the clumping factor of 10 to no clumping factor, and find that it does indeed enhance H_2 formation. Others employ a variable density-based clumping factor (Tomassetti et al. 2014; Lupi et al. 2018). Tomassetti et al. (2014) find that their model with the constant clumping factor is closer to the KMT equilibrium model compared to the variable clumping factor. Others opt out of the clumping factor completely (Baczynski et al. 2015; Hu et al. 2016; Richings & Schaye 2016; Pallottini et al. 2017).

The second choice is whether or not to link star formation explicitly to H_2. Indeed, star formation is observationally correlated to H_2 (McKee & Ostriker 2007), but this may be because both stars and H_2 form in dense cold environments and not because H_2 directly triggers star formation (Glover & Clark 2012). Gnedin & Kravtsov (2011) argue that by setting the SFR proportional to the H_2 density, as opposed to total gas density as is traditional, they avoid possibly arbitrary density and temperature thresholds since H_2 naturally correlates with dense, cold gas. Christensen et al. (2012), Tomassetti et al. (2014), and Pallottini et al. (2017) follow suit. Richings & Schaye (2016), Hu et al. (2016), Katz et al. (2017), Capelo et al. (2018), and Lupi et al. (2018), however, maintain an SFR proportional to total gas density. Hu et al. (2016) find in their simulations that star formation correlates with H I-dominated cold gas better than H_2, and see a significant quantity of warm, non-star-forming H_2 gas. Lupi et al. (2018) argue that the link is unnecessary because the KS relation between H_2 and SFR arises naturally without it.

A number of simulations that study molecular clouds in detail also include H_2 chemistry. Dobbs et al. (2008) use a non-equilibrium chemical network (Bergin, Hartmann & Raymond 2004), a constant dissociation rate for H_2, and to calculate column density they adopt a constant length that represents the typical distance to a B0 star. This framework is also adopted by Khoperskov et al. (2013), and Khoperskov et al. (2016) introduce ray tracing, while Duarte-Cabral & Dobbs (2016) use radiative transfer post-processing.

In this paper, we employ RAMSES-RT (Rosdahl et al. 2013), which builds on the original RAMSES adaptive mesh refinement (AMR) code (Teyssier 2002) by adding radiative transfer for photon groups coupled to the non-equilibrium chemistry of H I, H II, He I, He II, and He III. In Nickerson, Teyssier & Rosdahl (2018), we added the non-equilibrium chemistry of H_2 coupled to the radiative transfer. We tested this code in a number of idealized situations in order to successfully compare it against analytical solutions where they existed and other codes where they did not. Most notably, we matched our results to benchmark tests in photodissociation region (PDR) codes (Röllig et al. 2007). The only adjustable parameter was in our novel self-shielding model for H_2, which took advantage of the radiative transfer. This was set by PDR scales smaller than those in use for galaxy simulations. We will not use a clumping factor in order to fully study the effects of resolution on H_2 content.

We use our model for molecular, atomic, and ionized hydrogen coupled to radiative transfer in an isolated Milky Way-like disc galaxy at three resolutions. We aim to show that our model, calibrated on the chemical scale, gives rise to H_2 relations on the galactic scale without any tuning on this larger scale. The layout is as follows. Section 2 describes the set-up and physics of our simulations. We demonstrate our model's fidelity to realism on the galactic scale for the high-resolution run and how resolution

affects the molecular gas content of our galaxy in Section 3. In Section 4, we employ a clump finder to identify molecular clouds to recover the Larson relation and cumulative mass profiles similar to observed molecular cloud populations. We discuss and summarize our findings in Section 5.

2 SIMULATION SET-UP

We will first describe the initial conditions for our isolated Milky Way-like disc galaxy, before summarizing the physics and chemistry critical to this work.

2.1 Initial conditions

We study an isolated Milky Way-like galaxy originally generated for the AGORA comparison project (Kim et al. 2014, 2016) at three resolutions, referred to as GHigh, GMed, and GLow. The square box width is 400 kpc. The dark matter halo initially follows a Navarro, Frenk & White (1997) profile, while the stellar and gas discs follow exponential profiles, and the stellar bulge follows a Hernquist profile (Hernquist 1990). The parameters are summarized in Table 1; most apply to all three galaxies, while the particle number and cells size depend on the resolution. Each galaxy evolves to 800 Myr, more than enough time to settle into a semi-steady state as discussed in Section 2.4.

2.2 RAMSES-RT

We simulate our galaxies with RAMSES-RT (Rosdahl et al. 2013; Rosdahl & Teyssier 2015), the radiative transfer extension of the hydrodynamics code RAMSES (Teyssier 2002). RAMSES uses AMR to model the gas with a second-order Godunov scheme and a N-body particle-mesh solver for dark matter and star particles. Our coarsest level is 7, and we refine up to levels 12, 14, and 16 for GLow, GMed, and GHigh, respectively. Following a quasi-Lagrangian scheme, a cell is refined if it has 10 or more dark matter and star particles older than 10 Myr, or if its combined gas and new stellar mass exceeds 10 m_* (defined in Table 1).

RAMSES-RT couples the hydrodynamics to the moment-based radiative transfer of photons using the M1 closure relation (Levermore 1984). In particular, photons are split into discrete frequency groups depending on which species they dissociate or ionize, and their properties are integrated over the entire frequency range of the group. We use the reduced speed of light approximation (Gnedin & Abel 2001) in order to decrease computational time, specifically $c_r = c/200$ as in Rosdahl et al. (2015) for galaxy simulations.

2.3 Gas chemistry

The chemical prescription we use here is the molecular hydrogen addition to RAMSES-RT (Nickerson et al. 2018). We track the non-equilibrium chemistry of H_2, H I, H II, He I, He II, and He III tied to the four dissociating and ionizing photon groups given in Table 2. Details of the molecular chemistry are given in Nickerson et al. (2018) and the ionization chemistry in Rosdahl et al. (2013) but we summarize the processes here.

Our H_2 model includes the formation of H_2 on dust (Jura 1974; Hollenbach & McKee 1979; Gry et al. 2002; Habart et al. 2004), as well as formation in the absence of dust via the gas phase (McKee & Krumholz 2010) and three-body collisions (Palla, Salpeter & Stahler 1983; Forrey 2013), destruction by collision with H I (Dove & Mandy 1986) and with itself (Martin, Keogh & Mandy 1998), photodissociation by the Lyman–Werner band (i.e. Group 1) (Sternberg et al. 2014), photoionization (Abel et al. 1997), and ionization by cosmic rays (Glassgold & Langer 1974; Indriolo & McCall 2012; Gong, Ostriker & Wolfire 2017). In particular, we use a shortcut for the H_2 ionization. Instead of tracking the resultant species H_2^+, we treat H_2 ionization as a dissociation that creates two H I atoms, under the assumption that an environment that ionizes H_2 is going to quickly ionize H I. The H I and He chemistry involves formation by recombination (Hui & Gnedin 1997), collisional ionization (Cen 1992), photoionization (Verner et al. 1996; Hui & Gnedin 1997), and cosmic ray ionization (Glassgold & Langer 1974; Glover et al. 2010; Indriolo et al. 2015; Gong et al. 2017). We assume a hydrogen mass fraction of 0.76 and a helium mass fraction of 0.24.

The gas is heated by photodissociation and ionization, the photoelectric effect (Bakes & Tielens 1994; Wolfire, Mckee & Hollenbach 2003), UV pumping from LW absorption that does not lead to H_2 dissociation (Burton, Hollenbach & Tielens 1990; Draine & Bertoldi 1996; Baczynski et al. 2015), H_2 formation heating (Hollenbach & McKee 1979; Omukai 2000), and heating by cosmic ray ionization (Glassgold, Galli & Padovani 2012). Gas is cooled by collisional ionization (Cen 1992), collisional excitation (Cen 1992), recombination (Hui & Gnedin 1997), dielectronic recombination (Black 1981), bremsstrahlung cooling (Osterbrock & Ferland 2006), Compton cooling (Haiman, Thoul & Loeb 1996), metal cooling by CLOUDY (Ferland et al. 1998) above 10^4 K and fine structure cooling (Rosen & Bergman 1995) below 10^4 K, and H_2 cooling (Hollenbach & McKee 1979; Halle & Combes 2013).

Photons are created through stellar injection based on stellar energy distribution (SED) tables for stellar population models. Each star particle in RAMSES represents an entire population of stars. The quantity of photons injected into each photon group is determined by the mass, age, and metallicity of the star particle, and is calculated from the Bruzual & Charlot (2003) SED tables (see Rosdahl et al. 2013). Photons are absorbed by dust, the photoelectric effect, and gas via either photodissociation or ionization.

Self-shielding of H_2 is vital to its formation. H_2 dissociation occurs by line absorption in the LW band, where first, only 10 per cent of absorptions lead to dissociation (Stecher & Williams 1967), and secondly, interference between absorption bands of differing strengths leads to decreasing H_2 destruction with increasing column density (Draine & Bertoldi 1996). Previous galaxy codes with H_2 have modelled this effect by decreasing H_2 destruction and using an approximation to convert volume density in the code to a column density (Wolcott-Green, Haiman & Bryan 2011), with the exception of Baczynski et al. (2015), who use a ray-tracing code. What we do instead is to enhance LW destruction at each time-step but not H_2 dissociation, and thereby do not require a conversion to column density because the LW photons will travel through the column of cells with each time-step. We calibrate the factor of LW destruction enhancement with one-dimensional simulations of radiation dissociating an H_2 slab (see Nickerson et al. 2018). We compare our transition between H_2 and H I with its position as predicted by the analytical model of Bialy et al. (2017), and find that enhancing the LW destruction by a factor of 400 gives good results for a range of incident fluxes, slab densities, and metallicities (Nickerson et al. 2018).

Our homogeneous ultraviolet (UV) background (Faucher-Giguère et al. 2009) is dampened above densities of 10^{-2} cm^{-3} to mimic gas self-shielding.

Table 1. Galaxy parameters for the three resolutions of galaxies, which are labelled: GHigh, GMed, and GLow. Parameters that apply to every galaxy fall under the 'All' column, and those that differ fall under the column for each resolution. The dark matter halo parameters are as follows: M_{200}: halo virial mass is defined as the mass within a sphere 200 times more dense than the Universe's critical density, v_{c200}: circular velocity inside this sphere, r_{200}: radius of this sphere, c: concentration parameter, λ: the spin parameter, and N_{dm}: the number of dark matter particles. The stellar component parameters are as follows: M_{*disc}: mass of the stellar disc, r_{disc}: radius of the disc, N_{*disc}: the number of star particles in the disc, B/D: bulge-to-disc mass ratio, N_{*bulge}: the number of star particles in the bulge, n_*: star formation critical density, and m_*: the mass of a new star particle. The gas disc properties are as follows: f_{gas}: gas fraction of the disc mass of gas and stars, Z_{init}: initial metallicity, Δx_{min}: minimum AMR resolution cell size, and Δx_{max}: maximum AMR resolution cell size.

Component	Parameter		All	GHigh	GMed	GLow
Dark Matter Halo	virial mass	M_{200}	1.074×10^{12} M$_\odot$	–	–	–
	circular velocity	v_{c200}	150 km s^{-1}	–	–	–
	virial radius	r_{200}	205.4 kpc	–	–	–
	concentration	c	10	–	–	–
	spin	λ	0.04	–	–	–
	particle number	N_{dm}	–	10^7	10^6	10^5
Stars	stellar disc mass	M_{*disc}	4.297×10^{10} M$_\odot$	–	–	–
	disc radius	r_{disc}	3.432 kpc	–	–	–
	disc particle number	N_{*disc}	–	10^7	10^6	10^5
	bulge-to-disc ratio	B/D	0.1	–	–	–
	bulge particle number	N_{*bulge}	–	1.25×10^6	1.25×10^5	1.25×10^4
	star formation threshold	n_*	–	300 cm^{-3}	50 cm^{-3}	8 cm^{-3}
	new particle mass	m_*	–	10^3 M$_\odot$	10^4 M$_\odot$	10^5 M$_\odot$
Gas Disc	disc gas fraction	f_{gas}	20 per cent	–	–	–
	initial metallicity	Z_{init}	1 Z$_\odot$	–	–	–
	min resolution cell size	Δx_{min}	3125 pc	–	–	–
	max resolution cell size	Δx_{max}	–	6.1 pc	24 pc	97 pc

Table 2. The photon group properties in our simulations, where $h\nu$ is the photon energy.

Group number	Min $h\nu$ (eV)	Max $h\nu$ (eV)	Purpose
1	11.20	13.60	H_2 dissociation
2	13.60	24.59	H_2 and H I ionization
3	24.59	54.42	H_2, H I, and He I ionization
4	54.42	∞	H_2, H I, He I, and He II ionization

2.4 Star formation and feedback

We use the star formation model described in Rasera & Teyssier (2006) that follows a Schmidt (1959) law based on the total gas density. Gas above a critical density and below 3×10^4 K turns into star particles following

$$\dot{\rho}_* = \begin{cases} \epsilon_{ff}\rho/t_{ff} & n > n_*, \\ 0 & n \leq n_*, \end{cases} \quad (1)$$

where $\dot{\rho}_*$ is the rate of gas conversion into stars in units of mass per volume per time, $\varepsilon_{ff} = 0.02$ is our choice of local star formation efficiency, ρ is the gas density, $t_{ff} = \sqrt{3\pi/(32G\rho)}$ is the gas free-fall time, n_* is the star formation critical density, and G is the gravitational constant. The critical density for star formation (n_*) and resulting mass of each new star particle (m_*) depend on resolution (see Table 1) and the number of stellar particles formed in each cell in each time-step is randomly drawn from a Poisson distribution of the Schmidt (1959) law.

We use a delayed cooling model for stellar feedback as developed by Teyssier et al. (2013). At the age of 10 Myr, each star particle releases the energy, E_{SNII},

$$E_{SNII} = 10^{51} \frac{\eta_{SN} m_*}{M_{SNII}} \text{erg}, \quad (2)$$

where $\eta_{SN} = 0.3$ is the fraction of stellar mass released by supernovae, and $M_{SNII} = 10$ M$_\odot$ is the Type II supernova mass, close to Chabrier (2003). Our supernovae do not release metals. Delayed cooling is intended to offset the effect of numerical overcooling, whereby non-thermal energy is allowed to cool over a 20 Myr timescale.

Our ionization feedback is computed directly from the radiative transfer built into RAMSES-RT (Rosdahl et al. 2013). The effects of this method are detailed in Rosdahl et al. (2015), where ionization feedback reduces star formation and increases gas disc thickness in low-mass galaxies, but has less of an effect on Milky Way-mass galaxies such as the one in this work.

3 GALACTIC ANALYSIS

In this section, we focus on analysing three galaxies that differ by resolution: GLow, GMed, and GHigh. We present their SFR histories, morphologies, radial profiles, KS diagrams, phase diagrams, and the density and fraction distributions of H_2.

3.1 SFR history

We first show the discs' evolution over time. Fig. 1 gives the star formation history of GLow, GMed, and GHigh. The discs begin with a uniform exponential structure, and quickly evolve substructure. Star formation in all three simulations is initially high for 100–200 Myr, and then calms down as the disc settles into its semisteady state. GLow's SFR slowly decays over the course of 500 Myr until it reaches a semisteady state at about 800 Myr. GMed, on the other hand, settles much more quickly at about 500 Myr. GHigh reaches a semisteady state much faster following its initially high SFR at

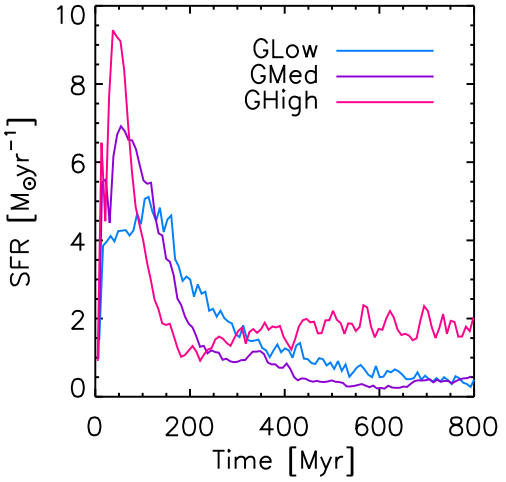

Figure 1. The star formation history of GLow (blue), GMed (purple), and GHigh (pink).

300 Myr, and settles into a much higher SFR as compared to GMed and GLow, marked by bursts of star formation.

We run GMed and GLow to 2 Gyr beyond what is shown here, in order ensure that 800 Myr is indeed a representative time of their equilibrium state. GHigh is too computationally expensive to run longer, but it has been stable for several hundreds of Myr. Accordingly, we choose 800 Myr as the time at which to analyse the galaxies.

3.2 Morphology

In Figs 2, 3, and 4, we provide maps for GLow, GMed, and GHigh face-on and side-on of the total gas density, H_2 fraction, H I fraction, gas temperature, H_2 total photodissociation and ionization rate, and density of stars born after the simulations' start. We do not include the H I photoionization rate because it follows the H_2 rate very closely, both sourced from young stars and absorbed by gas.

We define the maximum H_2 abundance fraction $x_{H2} = 0.5$ because H_2 is diatomic. In this work, we display $2 * x_{H2}$ so that its range from 0 to 1 is visually comparable to x_{HI} and x_{HII}.

The most obvious difference between the different resolution simulations first comes in the structure of the gas density. The gas is much more diffuse and the spiral arms fewer in GLow, while the complexity of the gas increases in GMed and GHigh. The high-density region, 10 cm^{-3} and higher, is confined to a smaller central core in GLow, and this is larger in GMed and GHigh. GHigh has more spiral arms, which are thinner, and filamentary structures, which are neither present in GMed nor GLow. The gas in GHigh has many more clumps, a subject we will return to in Section 4. The regions of high-density gas are also sharpest in GHigh, with a more distinct envelope of $\approx 10^{-3}$ cm^{-3} gas that ends sharply at $\approx 10^{-5}$ cm^{-3}. In the side-on maps, we can see material ejected above and below the disc by supernovae feedback. Very little is ejected in GLow, while streams of gas emit from GMed. GHigh has the most elaborate structure in its ejected gas, showing an additional fountain of high-density gas that soon falls back on to the disc.

The resolution differences in gas densities translate into differences in the H_2 and H I face-on maps. H_2 traces the densest regions in the galaxy, and accordingly increases in structural complexity with resolution. While GMed's H_2 map is a simple progression of GLow, being denser and having more arms, GHigh brings new features to the H_2 map. The outer H_2 regions are much thicker and diffuse, while the middle region has more numerous H_2-free pockets and thinner H_2 clouds as compared with GMed. The innermost disc returns to being continuously high in H_2 with a delicate spiral structure. H I is more spread out and evenly distributed than H_2 and is present in the inter-arm regions. It follows the same resolution effects as H_2, gaining structure with higher resolution, but gaining holes mid-disc in GHigh. H I traces the ejected gas and the galactic fountain as seen in the gas density maps, while H_2 is confined to the disc. This same effect is seen in the ISM box simulations of Girichidis et al. (2016).

The temperature map of GLow is much colder than that of GMed or GHigh. GMed features cold clumps and arms with hotter inter-arm regions, while GHigh has more hot patches and a distinct cold, outer envelope. High-temperature regions envelop the young stars. The side-on view reveals that most of the cold gas remains in the disc in GLow and GMed. GHigh has a much richer side-on view, the disc showing a cold fountain of gas, also seen in H I, expelled from the disc.

The photodestruction maps follow the dissociating and ionizing radiation of the youngest stars and any supernovae, and accordingly tend to vary the most depending on which time-step we use. Generally, GHigh does have more stars and radiation spots of varying sizes spread throughout most of the disc. GMed has fainter radiation throughout the disc, while GLow has a brighter central concentration of stars as compared to GMed, but very little in the rest of the disc. The dark swathes in these maps correspond to the highs in the H_2 map, where it successfully shields against the photons. Side-on, this radiation leaks out above and below the disc, but very little penetrates the plane of the disc.

The stellar density map includes all stars born after the simulation began and does not include any stars from the initial conditions. The density and structural complexity of the stellar map increase greatly with resolution. Spiral structure is barely resolved in GLow with much fewer but more massive stars, but spirals and stellar clumps become apparent in GMed, with GHigh featuring an even grander spiral structure. When considering the side-on views, all these new stars are confined to the disc, while the bulge (not shown here) comprises entirely stars from the initial conditions.

3.3 Galactic observables

In this section, we aim to provide the observable features of our galaxies. We compare our simulations to nearby galaxy measurements in the THINGS survey of H I (Walter et al. 2008) and the molecular surveys HERACLES (Leroy et al. 2009) and BIMA SONG (Helfer et al. 2003) combined in Bigiel et al. (2008). We bin the radial profiles of our galaxies into 0.5 kpc wide cylindrical segments and take the SFR over an average of 200 Myr as recommended by Gnedin & Kravtsov (2011) for comparing simulations to these measurements.

First, we present the radial profiles for our three galaxies in H_2, H I, and SFR surface densities in Fig. 5. Our goal is not to reproduce any one specific galaxy but to ensure that our galaxies are morphologically feasible. We compare our galaxies to the radial profiles provided in Leroy et al. (2008) and Gallagher et al. (2018). The general trend in their observations is for H_2 and SFR to follow one another, peak at the galactic centre, and fall towards the outer disc, while H I is roughly constant throughout the disc. In the Leroy et al. (2008) galaxy sample, H_2 dominates in the centre and H I dominates the outer disc, while in the Gallagher et al. (2018) catalogue H_2 maintains dominance throughout the entire disc.

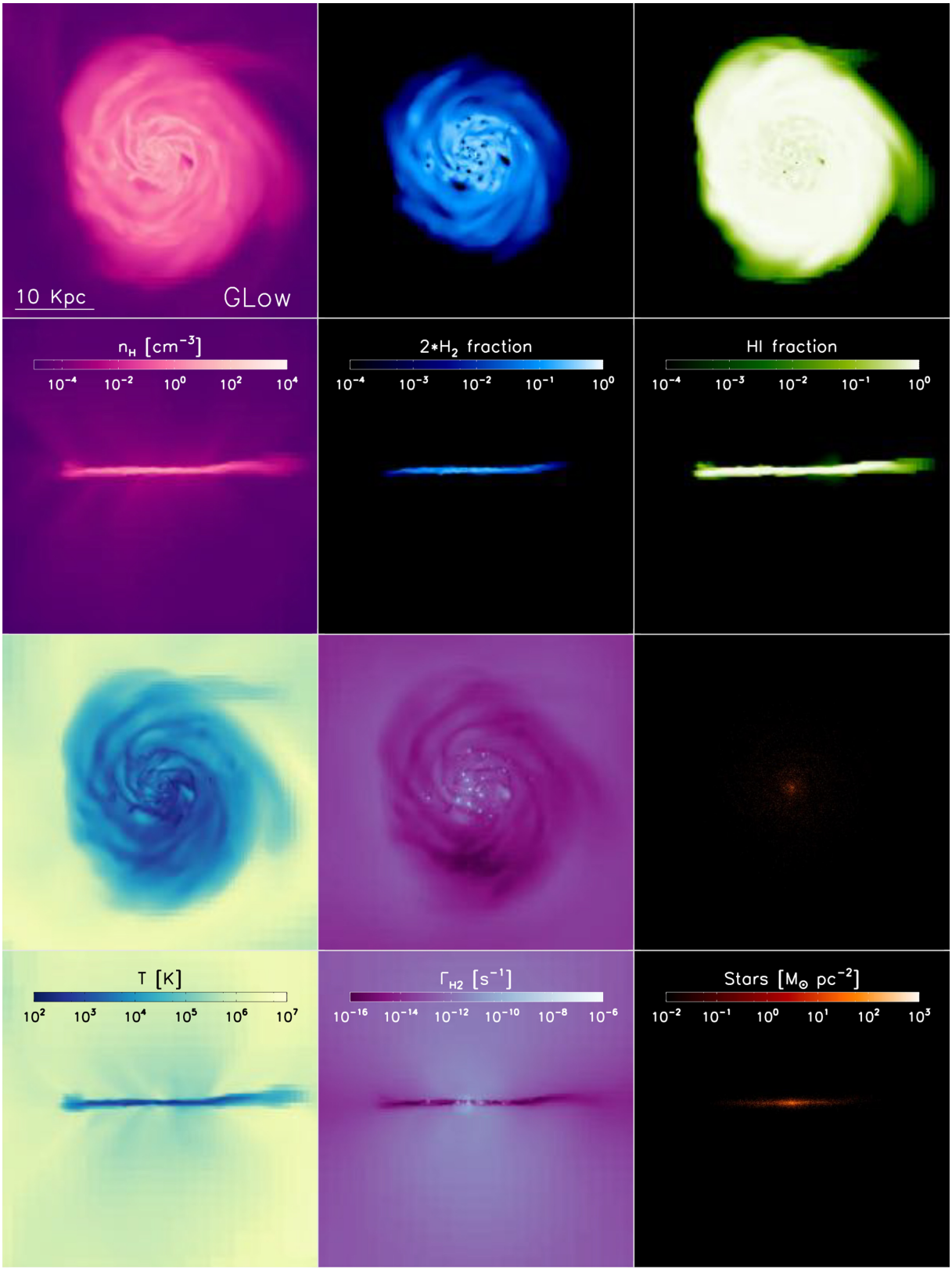

Figure 2. Face-on maps of GLow mass-weighted average over the disc height, and side-on maps over the disc width. Top row, left to right: face-on total gas density (cm^{-3}), H_2 fraction, and H I fraction. Second from the top row: same as the top row, side-on. Second from the bottom row, left to right: face-on gas temperature (K), H_2 photodissociation plus photoionization rate over all groups (s^{-1}), and stellar density of stars born after simulation start ($M_\odot$ pc^{-2}). Bottom row: same as the second from the bottom row, side-on. The Habing value, G_0, in units of s^{-1} for the photodestruction rate is about 6×10^{-11} s^{-1}.

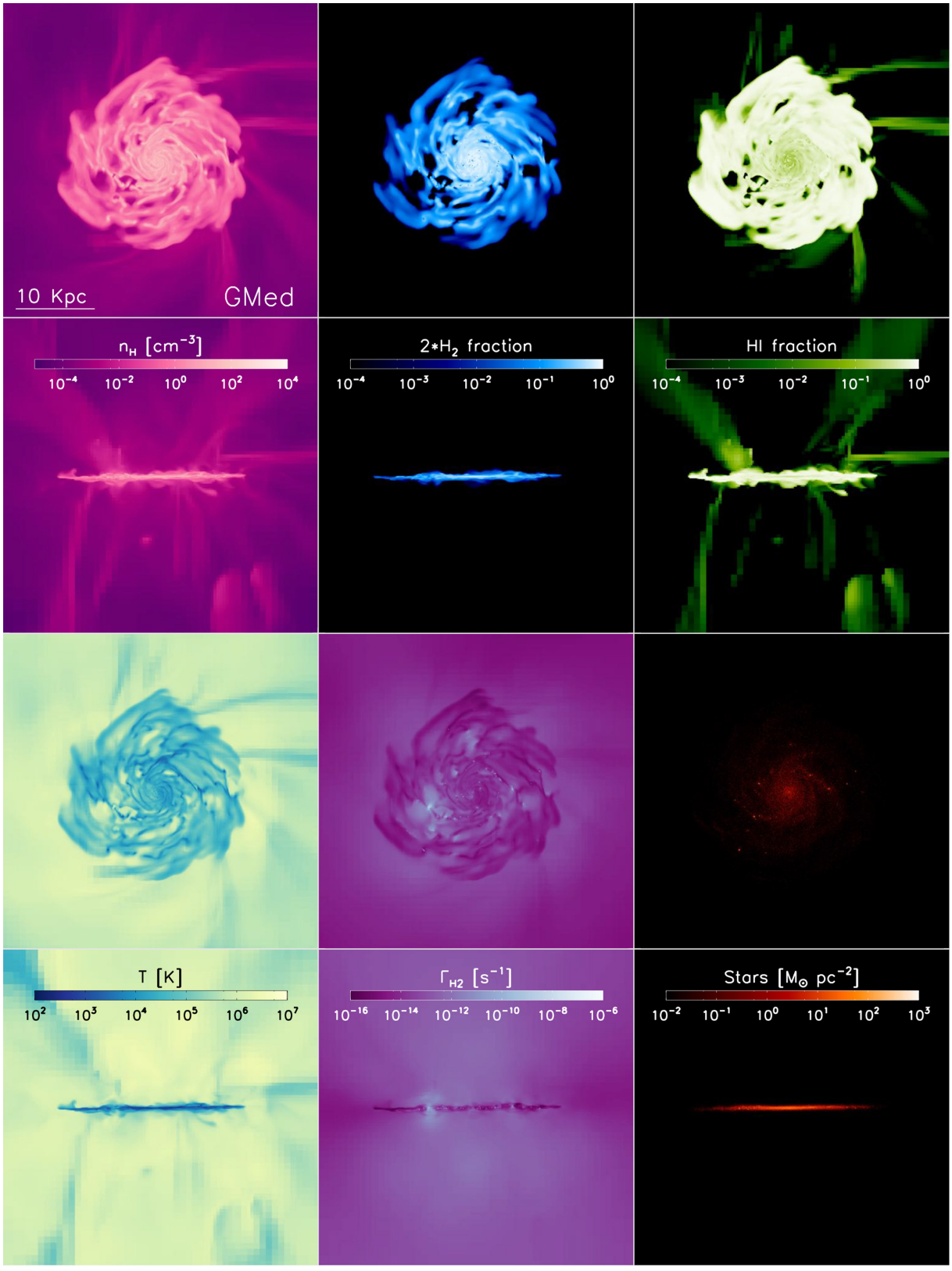

Figure 3. The same as in Fig. 2 for GMed.

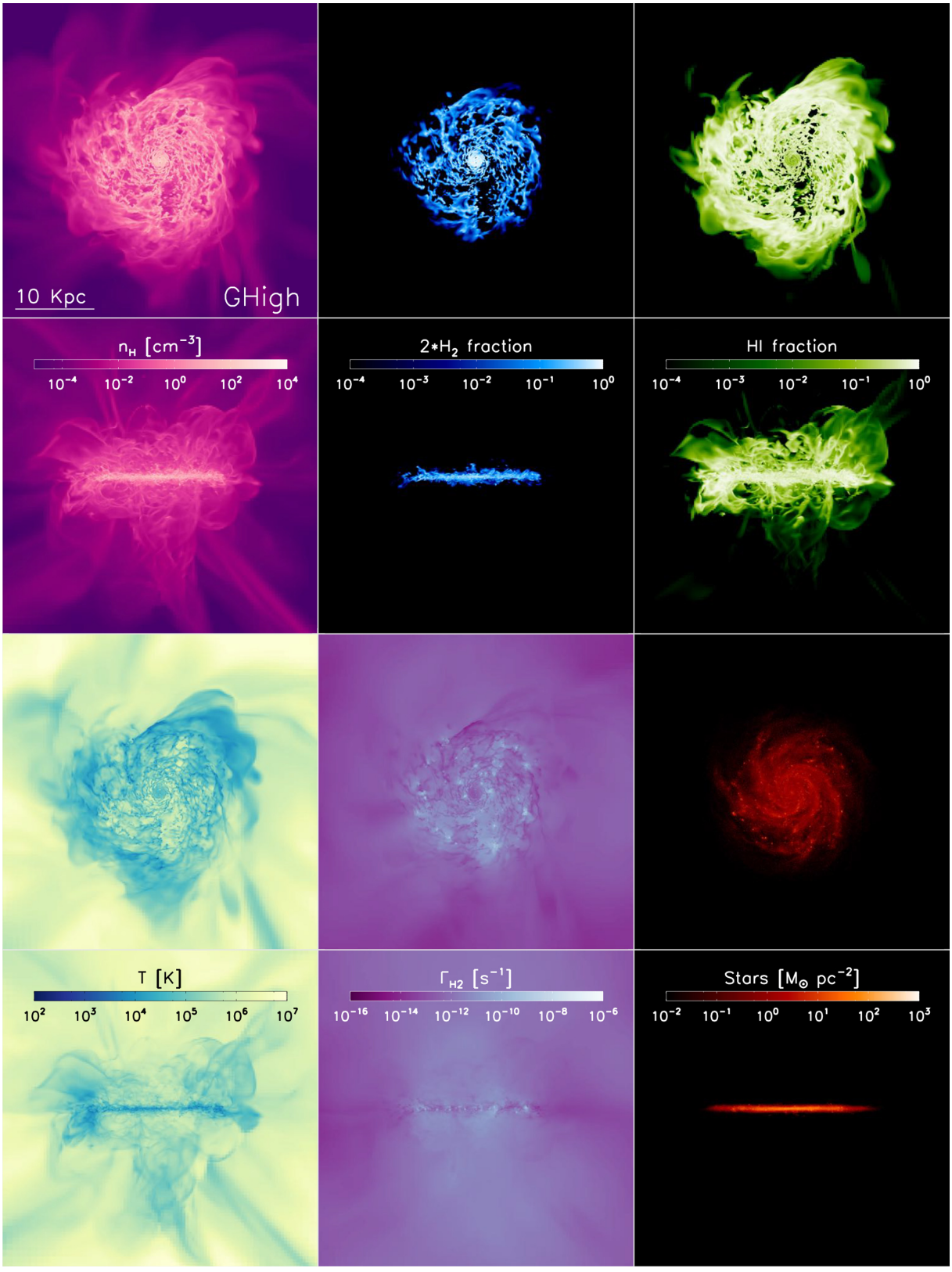

Figure 4. The same as in Fig. 2 for GHigh.

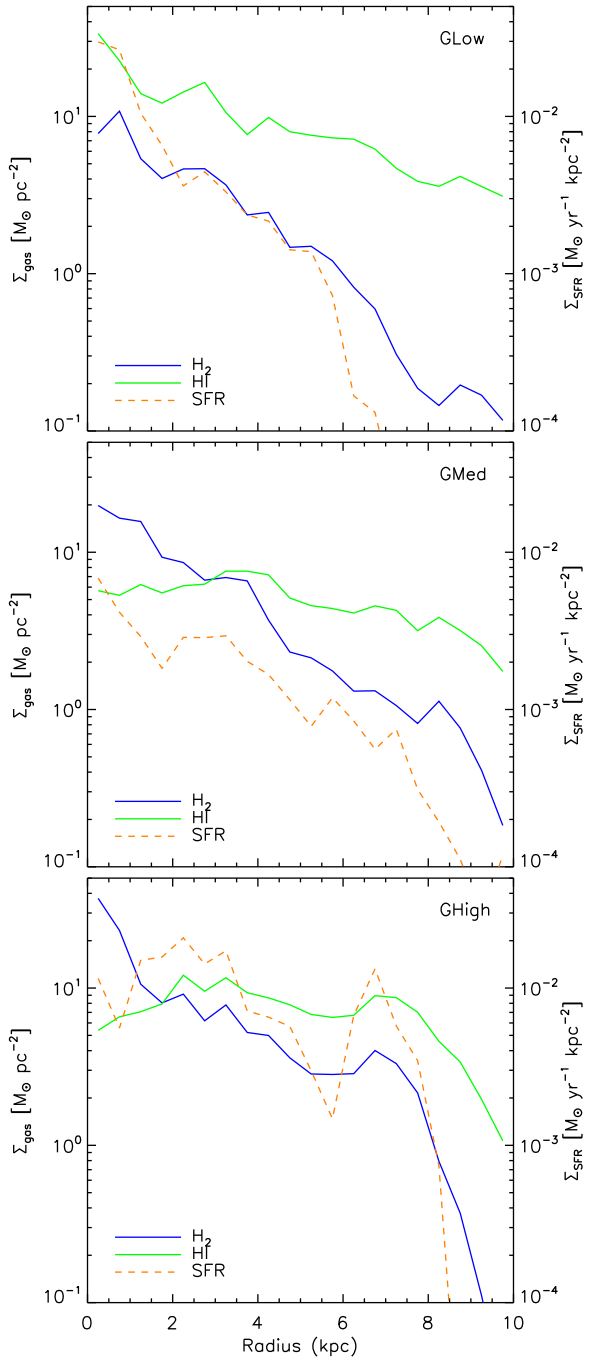

Figure 5. The surface density profiles of H_2, H I ($M_\odot$ pc^{-2}), and SFR ($M_\odot$ yr^{-1} kpc^{-2}) for GLow, GMed, and GHigh in 0.5 kpc bins. The SFR is averaged for 200 Myr.

With our galaxies in Fig. 5, it is clear that resolution affects the profiles greatly. In GLow, the surface density of H_2 never overtakes H I and remains low. Furthermore, the SFR peaks in the centre much higher than GMed and GHigh and drops rapidly mid-disc. This high central SFR is probably because GHigh has a bulge with more particles than GMed and GLow (Table 1). This leads to morphological quenching in which the bulge stabilizes the gas disc against star formation (Martig 2009). GMed and GHigh resemble the features of observed galaxies much more closely, especially the Leroy et al. (2008) galaxies. In both, the H_2 peaks in the galactic centre and falls towards the outer disc, while the H I profile remains relatively flat throughout the disc. The SFR also peaks in the centre for GMed, while GHigh's SFR does not centrally peak but does have higher central H_2 compared to GMed. In all three of our galaxies, the trends in SFR do largely follow H_2.

In Fig. 6, we show the KS relation (Schmidt 1959; Kennicutt 1998) for our galaxies as compared to the data downloaded from Bigiel et al. (2008). This snapshot at 800 Myr is typical of the relation across many snapshots for the semistable state of the disc.

First, we give the traditional relation between the surface densities of total neutral hydrogen and SFR, and then we show the same relation between the surface densities of H_2 and the SFR. It is clear in both the relations that GLow follows a different slope than GMed and GHigh. GHigh is a higher SFR version of GMed, sharing similar slopes. Also, in both the relations, our simulated galaxies fall within the margins of the observational data. Our simulations extend to much lower densities than is possible with Bigiel et al. (2008)'s instrumentation, but we cannot resolve surface densities as high as the observations, and so observation and simulation meet in the middle. In the total neutral gas relation, we reproduce not only the linear correlation at higher densities but also its breakdown at lower densities. This breakdown is not visible in the Bigiel et al. (2008) data, but is present in the later Schruba et al. (2011) data, which goes to lower surface densities. However, in the H_2 relation each galaxy is able to maintain a roughly constant linear relation at all densities. The exception is two central points in GHigh, where our central SFR is morphologically quenched despite high Σ_{H_2}. Our simulated galaxies reproduce the tighter correlation between the molecular gas and SFR as compared to neutral gas that is seen in observation.

Summing the total H_2 fraction of neutral gas for GLow, GMed, and GHigh, we have 0.14, 0.35, and 0.33. The H_2 fraction of neutral gas within the solar circle (defined as 7 kpc) is about 0.25–0.29, taking the H_2 mass as estimated by Heyer & Dame (2015) and H I mass measured by Sofue (2018). GMed and GHigh are close to this, while GLow greatly underestimates the molecular content. Another way to slice the data is to take the ratio of H_2 mass to H I mass, where we find for GLow, GMed, and GHigh values of 0.17, 0.55, and 0.49, respectively, which all fall into the range for disc galaxies in the COLD GASS survey by Boselli et al. (2014), about 0.03–10.

3.4 Phase diagrams

In Fig. 7, we present the phase diagrams for temperature, H II fraction, H I fraction, and H_2 fraction versus total hydrogen gas density, and mark our star formation density. Star formation always occurs in our simulation below 3×10^4 K, and the density threshold changes depending on the resolution (Table 1). Every diagram is weighted by gas mass.

Our n_H–T diagram shows the characteristic multiphase nature of these galaxies. The strongest feature shows increasing temperatures at lower densities, reaching as high as 10^7 K at 10^{-6} cm^{-3}, a constant temperature of about 10^4 K at intermediate densities around (10^{-4})–(10^{-2}) cm^{-3}, and dropping at higher densities to approximately 10^2 K in GLow, $10^{1.5}$ K in GMed, and a little over 10 K in GHigh. At $\approx 10^{-2}$ cm^{-3}, the sparse region of gas hotter than 10^4 K is caused by SN feedback and increases in prevalence with increasing resolution.

The H II fraction is 1 at the lowest densities, and at all resolutions its transition to 0 begins at 10^{-2} cm^{-3} and ends at $\approx 10^0$ cm^{-3}. The spread in the intermediate fractions at higher densities increases with increasing resolution, and is probably due to the SN feedback.

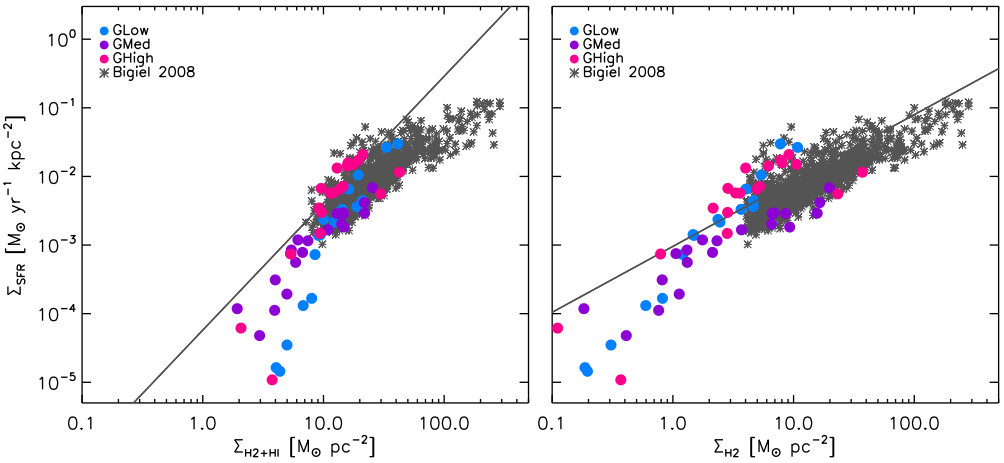

Figure 6. The KS relation for GLow (blue), GMed (purple), and GHigh (pink) in 0.5 kpc bins. The SFR averaged for 200 Myr. Our simulations are compared to the data from Bigiel et al. (2008) given by the grey stars, and the grey line is the power law that they derive.

The H I fraction is 0 at the lowest densities but begins to increase with increasing densities following H II's decrease after 10^{-2} cm^{-3} due to damping the UV background. However, the H I fraction climaxes at about 0.95, and its rise halts at a little after 10^{0} cm^{-3}, where it begins to decline. As we pass the star formation threshold, there is again an increase in H I at higher fractions.

The H_2 fraction completes the picture. At every resolution, H_2 begins forming at densities higher than 10^{-2} cm^{-3} and its fraction climbs with increasing density until reaching the star formation threshold where it drops back down to 0. Of all the hydrogen species, the H_2 abundance is most affected by resolution. In GLow, it only goes as high as 0.70, in GMed 0.92, and in GHigh 0.985.

Comparing the H I–H_2 transition to simulations in other works is difficult because of the number of factors involved. It can vary within the same code and model depending on the dust or UV flux (Gnedin & Kravtsov 2011; Hu et al. 2016) or metallicity (Christensen et al. 2012; Pallottini et al. 2017). Instead, we can look at the total H_2 fraction that different codes achieve. As in this work, Tomassetti et al. (2014)'s cosmological simulations do not form 100 per cent molecular gas in their non-equilibrium model. Other simulations by Gnedin & Kravtsov (2011), Christensen et al. (2012), Hu et al. (2016), Capelo et al. (2018), and Lupi et al. (2018) are able to form regions of 100 per cent H_2, but many of these codes use a clumping factor to enhance H_2 formation and account for unresolved substructure. Our philosophy is to not use this clumping factor. Instead, we seek to explain the cause of our simulations' inability to form 100 per cent molecular regions.

This stems from unresolved Strömgren spheres (Strömgren 1939), which is the hot, ionized gas from young stars. This problem was first described in Rosdahl et al. (2015) in the context of unresolved H II regions. These regions are present in the top row of Fig. 7 as diagonal streaks in the star formation region at the highest densities, and are most obvious in GHigh. In the n_H–T diagram, this is the shorter, higher temperature branch above the main star formation branch, and in the n_H–x_{HII} diagram this is the increase in H II fraction with decreasing densities that stops at the star formation threshold. In reality, the Strömgren sphere around a new star should be entirely ionized with a negligible atomic shell embedded in an entirely molecular region, as demonstrated with our code in Nickerson et al. (2018). However, even in GHigh the resolution goes only down to 6.1 pc, much larger than what many of the Strömgren spheres would be around our star particles. This instead produces a cell that is mostly atomic with a smidge of ionized and molecular hydrogen. Unfortunately, given our current star formation model we cannot resolve these small regions, as detailed in Rosdahl et al. (2015).

We can correct this with post-processing. We consider only cells with stars younger than 10 Myr, the age at which they produce a supernova. Using the SED tables (Bruzual & Charlot 2003), we can calculate the Strömgren radius of all stars in a cell, using equation (62) in Nickerson et al. (2018). If this radius is less than the distance from the cell centre to the outer corner then in post-processing we split the cell into two regions. The volume inside the radius is considered to be completely H II, since H I is negligible, while the region outside is considered to be completely H_2. Fig. 8 gives the results of this post-processing for GHigh. The high H II fraction above the star formation threshold completely disappears, while there is a lower concentration of H I, and we obtain a completely molecular fraction at high densities.

We take this post-processing technique further in applying it to the radial profiles in Fig. 5 and the KS relation in Fig. 6. Despite the cells with unresolved Strömgren radii being the densest, they actually have a negligible impact on the overall galactic morphologies. It appears that even though we do not resolve the regions around new stars and the completely molecular region, it has little impact on the overall results.

3.5 Molecular distribution

As our 'Introduction' section highlights, H_2 is difficult to observe directly and instead a tracer of even denser gas, CO, is used to convert to H_2 abundance. There is observational evidence for dark molecular gas (coined by Wolfire, Hollenbach & Mckee 2010) that is not traced by CO (Grenier, Casandjian & Terrier 2005; Burgh, France & McCandliss 2007; Roman-Duval et al. 2010). From the theory side, Wolfire et al. (2010) estimate that about 30 per cent of H_2 is dark and Smith et al. (2014) 42 per cent. While our own simulations do not include CO, we can none the less quantify the locations of our H_2 content.

In Fig. 9, we show the cumulative mass function of H_2 for every cell at all three resolutions versus twice the molecular fraction, the total gas density, and the temperature. Table 3 quantifies these results, showing the fractions, densities, and temperatures below which 25, 50, 75, and 100 per cent of H_2 mass is contained. In the

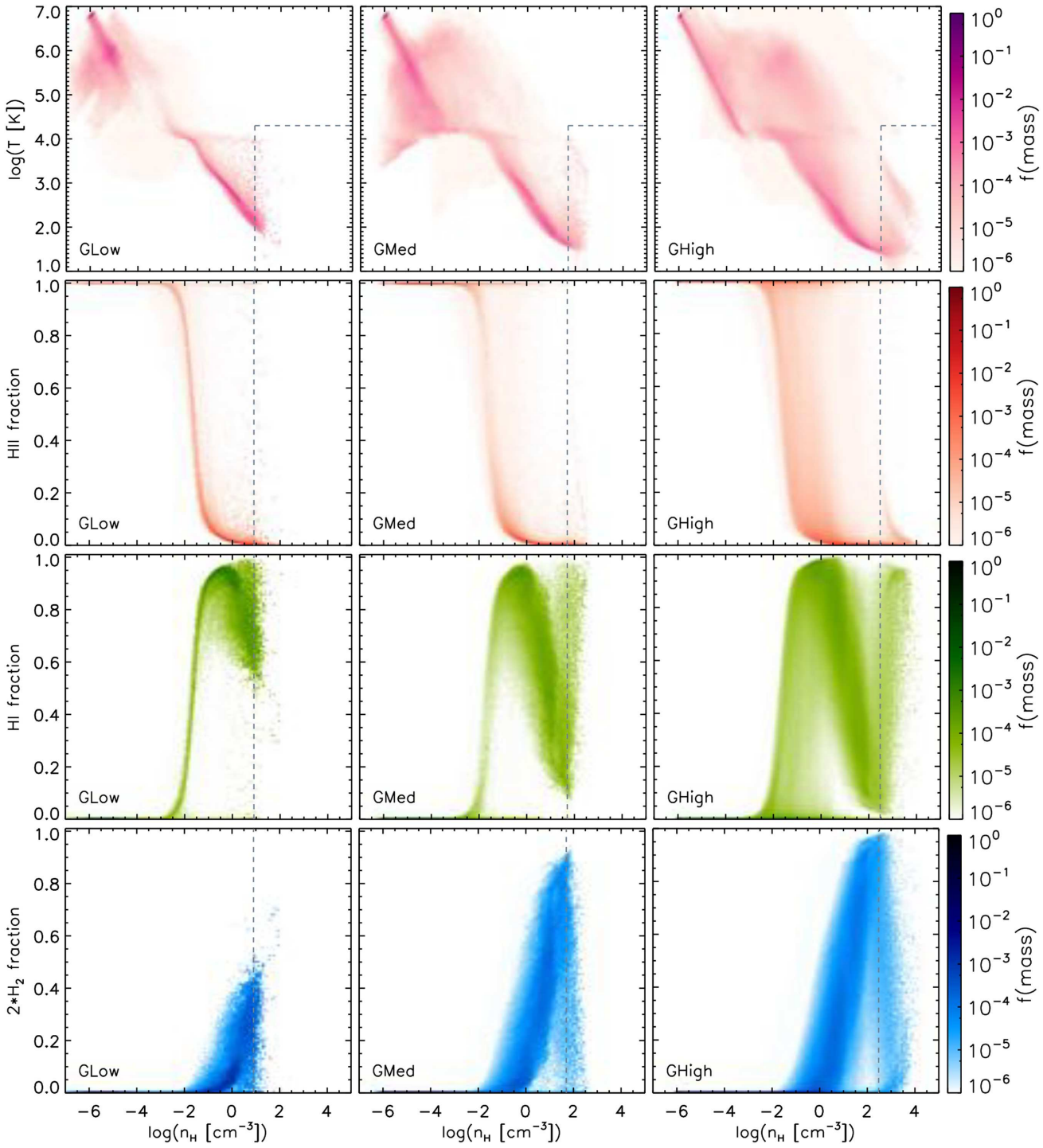

Figure 7. Phase diagrams of temperature (K) (top row), ionized hydrogen fraction (second from the top row), atomic hydrogen fraction (second from the bottom row), and twice molecular hydrogen fraction (bottom row) versus hydrogen gas density (cm^{-3}), left to right of: GLow, GMed, and GHigh. The star-forming region lies right of the dotted line, and in the temperature diagram below the dotted line.

cumulative function for molecular fraction, GLow has drastically less H_2 gas, while the GMed curve follows that of GHigh with a little less H_2. This echoes the findings in Duarte-Cabral & Dobbs (2016) where higher resolution is needed for higher molecular fractions. All three resolutions follow the same curve for the cumulative density function, with increasing resolutions reaching higher densities. The temperature distribution follows the results of the phase diagrams in Fig. 7. The majority of H_2 gas at every resolution is at $\sim 10^2$ K and lower, and higher resolutions resolve lower temperatures.

Table 3 shows that a significant fraction of H_2 exists in mixed regions, in which half of the gas is only 25.4, 50.7, and 57.0 per cent H_2 or less for GLow, GMed, and GHigh, respectively. Half of the H_2 gas is in low density regions below 5.57, 12.0, and 37.8 cm^{-3} for GLow, GMed, and GHigh. Clearly, a significant fraction of

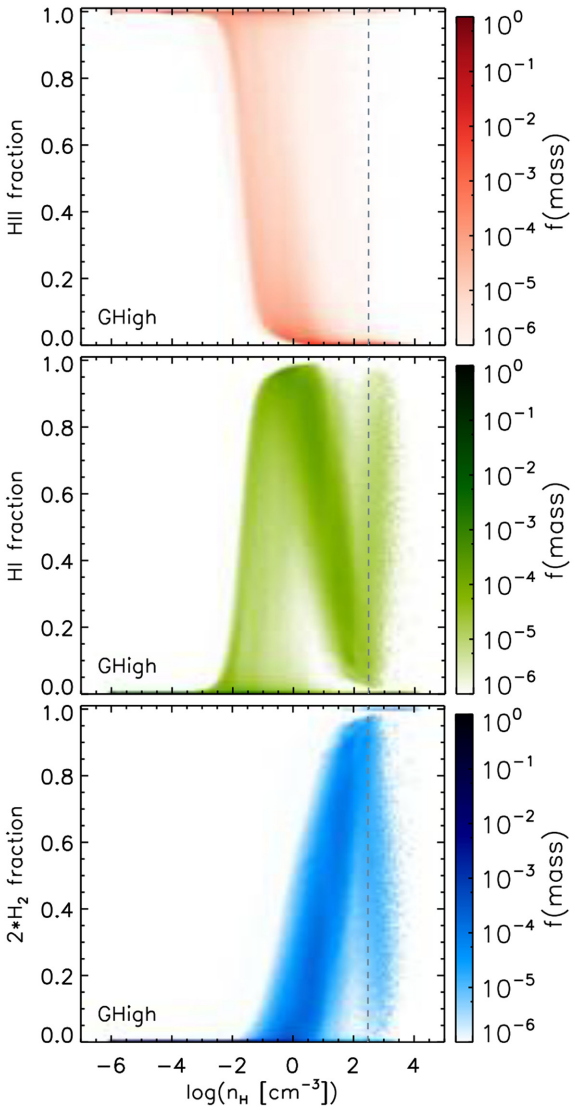

Figure 8. Post-processed phase diagrams to account for the unresolved Strömgren spheres for GHigh; top to bottom: ionized hydrogen fraction, atomic hydrogen fraction, and twice molecular hydrogen fraction versus hydrogen gas density (cm^{-3}). The star-forming region lies right of the dotted line.

our H_2 gas is in regions less dense than the average molecular cloud (see Fig. 13) and is significantly mixed with H I. The phase diagrams (Fig. 7) emphasize this as well, albeit in a more qualitative than quantitative fashion. Concerning temperature, 75 per cent of the H_2 is at temperatures of 343, 125, and 96.5 K and lower for GLow, GMed, and GHigh, respectively, supporting the findings by Cazaux & Tielens (2002) that H_2 formation is efficient for 300 K and lower. At each resolution, there exist cells at 10^6 K and higher, but these are rare and the H_2 in them will soon be destroyed.

4 MOLECULAR CLOUD ANALYSIS

Having looked at the overall properties of our galaxy, we now examine the molecular clouds within it. For this analysis, we use GHigh because only it has the resolution to study the clouds in satisfactory detail, the typical cloud density being 100 cm^{-3} (Dobbs et al. 2014). GLow and GMed, as seen in Fig. 7, are unable to form high enough gas densities in high enough quantities to be comparable to molecular clouds.

4.1 Clump finding and cloud properties

We identify the clouds using RAMSES' native clump finder Parallel Hierarchical Watershed (PHEW) (Bleuler et al. 2014), but base our search on H_2 density as opposed to total gas density. However, using the total gas density does not change the results. We set the density threshold as $n_{H2} = 50$ cm^{-3} (equivalent to $n_H = 100$ cm^{-3}) for a cell to be included in a cloud, which is the typical molecular cloud density (Dobbs et al. 2014), with a relevance threshold of 10. This density threshold for simulated molecular clouds is introduced in Tasker & Tan (2009). The saddle threshold above which two clumps are merged is 1000 cm^{-3}. We only consider clumps with at least 10 grid cells. The H_2 mass threshold is 10 $M_\odot$, a little higher than the lower limit observed in the Milky Way (Miville-Deschênes et al. 2017), though, as we will see in Fig. 12, our least massive cloud is actually of the order of 10^4 $M_\odot$ since the cell number is the more stringent factor.

Our clump finder PHEW works in position–position–position (PPP) space, which is native to simulations, while observations find clouds in position–position–velocity (PPV) space because the line of sight coordinate can only be obtained through velocity. Pan et al. (2015) show that both PPP and PPV analyses on the same simulation do produce similar cloud properties and structures. Grisdale et al. (2018) use a similar set-up to ours, with the RAMSES code, the AGORA Milky Way-like galaxy, and a resolution of 4.6 pc. They compare molecular clouds found with PPV to PPP (also with PHEW) and find that PPP clouds are a little more massive, denser, and the mass–radius and velocity dispersion–radius scaling relations steepen.

We consider only the molecular component when summing up each cloud's mass. The clump finder returns the volume of each cloud as summed over the individual cells that comprise it, and we calculate the radius by approximating each cloud as a sphere. We find the surface density via

$$\Sigma_C = M_C/(\pi R_C^2), \tag{3}$$

where Σ_C is the surface density, M_C is the total H_2 mass of the cloud, and R_C is the cloud radius.

A cloud's velocity dispersion is an important quantity, comprising the turbulent motion and the thermal components. For a comparison, we consider our clouds as observed face-on and use only the z-direction perpendicular to the galactic plane for calculating the turbulent velocity dispersion, $\sigma_{v,\mathrm{turb}}$:

$$\sigma_{v,\mathrm{turb}} = \sqrt{\frac{\sum_i m_{\mathrm{H2,i}}(v_{z,i} - \bar{v}_z)^2}{M_C}}, \tag{4}$$

where $\bar{v}_z$ is the H_2 mass-weighted mean velocity in the z-direction, i is the index of each cell in a cloud, $v_{z,i}$ is the z velocity of that cell, and $m_{\mathrm{H2,i}}$ is the H_2 mass in that cell. For the thermal component, we consider the sound speed, $\sigma_{v,\mathrm{therm}}$:

$$\sigma_{v,\mathrm{therm}} = \sqrt{\frac{\gamma k_B T_C}{\mu m_H}}, \tag{5}$$

where $\gamma = 5/3$ is the heat capacity ratio for this simulation, k_B is the Boltzmann constant, T_C is the H_2 mass-weighted average cloud temperature, μ is the mean molecular mass, and m_H is the mass of a hydrogen atom. Combining the two components, we acquire the

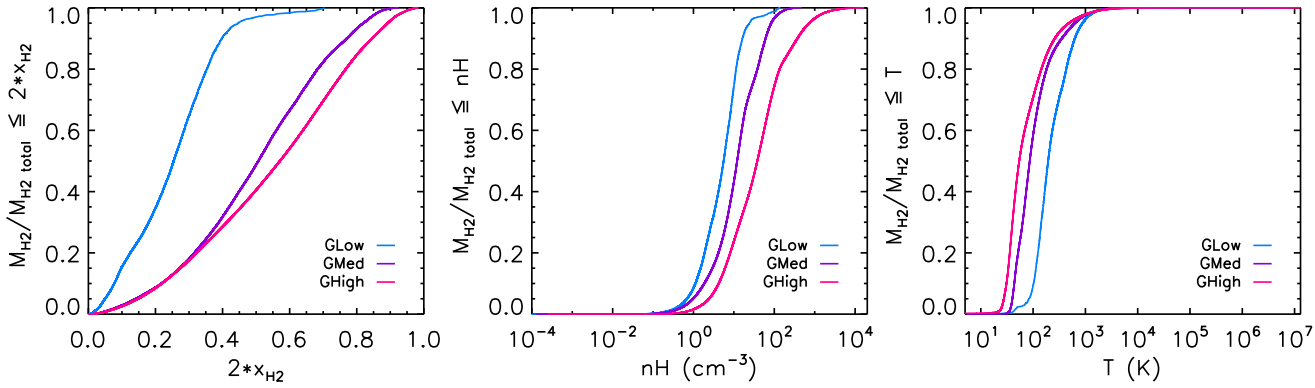

Figure 9. The cumulative distribution of H_2 mass at each resolution, as a fraction of total H_2 mass, left as a function of twice the molecular fraction, centre as a function of the total gas density (cm^{-3}), and right as a function of temperature (K).

Table 3. Distribution of total H_2 gas corresponding to Fig. 9. Columns left to right: quantity type (twice the H_2 fraction, the total gas density in cm^{-3}, or temperature in K); percentage of total H_2 mass at which the quantity is less than or equal to the values in the three columns to the right; GLow; GMed; and GHigh.

	$M_{H_2 total}$	GLow	GMed	GHigh
$2x_{H_2}$	≤25 per cent	0.155	0.354	0.368
	≤50 per cent	0.254	0.507	0.570
	≤75 per cent	0.334	0.652	0.734
	≤100 per cent	0.704	0.925	0.985
n_H (cm^{-3})	≤25 per cent	2.30	5.34	10.6
	≤50 per cent	5.57	12.0	37.8
	≤75 per cent	10.2	29.1	102
	≤100 per cent	143	476	1.70×10^4
T (K)	≤25 per cent	114	40.3	25.3
	≤50 per cent	171	65.8	39.7
	≤75 per cent	343	125	96.5
	≤100 per cent	1.81×10^6	8.91×10^6	1.22×10^7

total velocity dispersion, σ_v:

$$\sigma_v = \sqrt{\sigma_{v,\mathrm{turb}}^2 + \sigma_{v,\mathrm{therm}}^2}. \quad (6)$$

We note that, as expected for cold molecular clouds, the turbulent component dominates.

The dimensionless virial parameter α_{vir} (Bertoldi & McKee 1992) encapsulates the balance between gravitational and kinetic energy in a cloud:

$$\alpha_{vir} = \frac{2K_C}{|W_C|} = \frac{5\sigma_v^2 R_C}{GM_C}, \quad (7)$$

where K_C is the kinetic energy of the cloud, W_C is the potential energy of the cloud, and G is the gravitational constant. Clouds with $\alpha_{vir} \approx 1$ are considered to be in virial equilibrium, while clouds with $\alpha_{vir} > > 1$ need to be supported by internal pressure against the surrounding gas or are otherwise unbound and transient. $\alpha_{vir} < < 1$ means that a cloud requires a magnetic field support in order to maintain virial equilibrium (Bertoldi & McKee 1992), though we do not include magnetic fields in these simulations.

4.2 Cloud maps

Fig. 10 shows zoomed-in maps of our galaxy, both face-on and side-on, for total gas density, molecular hydrogen fraction, and total photodissociation and ionization rate for H_2 superimposed with the locations of our molecular clouds. We are unable to resolve clouds closest to the galactic centre but we resolve them for the remainder of the disc. They trace out the spiral arms, and the inter-arm region contains significantly fewer clouds.

Our clouds are part of a continuum of wider high-H_2 regions. Looking at the clouds side-on, they are mostly confined to the disc. The clouds are nearly entirely molecular with the average 96 per cent molecular, and the range is 93–97 per cent. The average H I fraction is 4 per cent and the average H II fraction is 0.04 per cent.

When comparing the clouds to the photon map, which traces the energy from young stars, it is clear that most of the clouds do not match these energy sources. We need to see, however, if any of the clouds that do align with the energy sources truly do, or if this is a projection effect. We calculate the nearest distance from each cloud to a young (≤ 10 Myr) star, and find that no young stars are within cloud radii. Fig. 11 shows a histogram of the distance of each young star to its nearest cloud's outer radius. This histogram is further divided into two cloud populations, inner and outer discs, for reasons we will elaborate on in Section 4.3. A negative value would imply that the star is inside the cloud, and this is satisfied by none of the clouds, the nearest being 68 pc away. This would suggest that once a cloud forms a star, the radiation quickly dissociates its high-density gas.

A further consequence of this is that we cannot produce SFR relations for our molecular clouds. However, Khoperskov & Vasiliev (2017) examine the KS relation on several scales for the same simulated galaxy, from 200 to 4 pc, and find that the KS relation breaks down 50 pc, which our lack of young stars in clouds supports.

4.3 Cloud comparison to observations and simulations

Cumulative mass functions for observed cloud masses are fitted either with a power law or truncated power law (Williams & McKee 1997). Most molecular cloud properties are remarkably uniform across different galaxies except for the cumulative mass function (Rosolowsky 2005). We present the cumulative mass function of our clouds in Fig. 12 and compare our simulated data to the fitted functions from three different galaxies: NGC 300 (Faesi, Lada & Forbrich 2018), the Milky Way (Rice et al. 2016), and M51 (Colombo et al. 2014). Being the least massive galaxy, NGC 300 harbours fewer and less massive clouds. Our galaxy, being a Milky Way analogue, does show a similar distribution of high-mass (10^7 $M_\odot$) clouds to the Milky Way, but we have a surplus of intermediate-mass clouds (10^6 $M_\odot$). The cumulative mass function

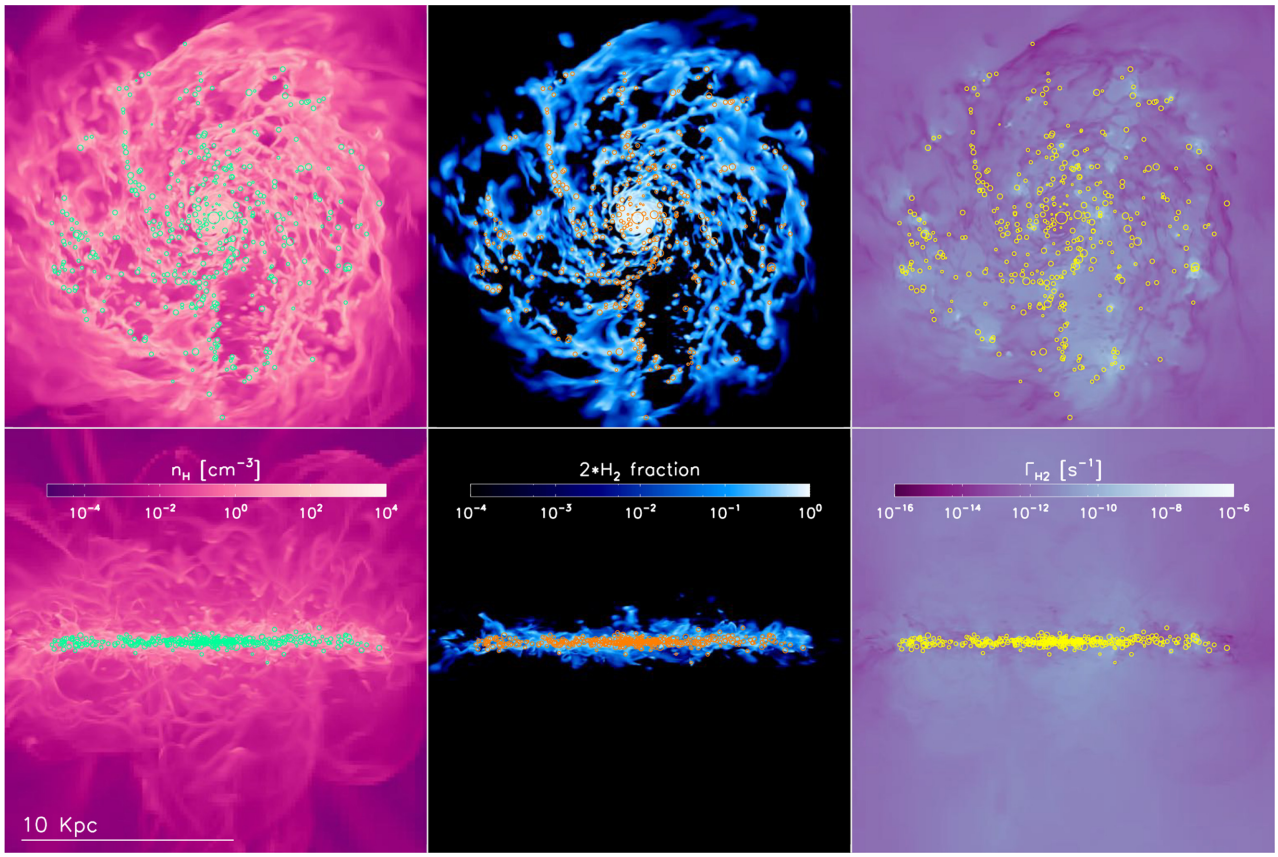

Figure 10. Positions of our clouds within GHigh, represented by the circles drawn at four times their radii, top row face-on and bottom row side-on, left to right, each property mass weighted: total gas density (cm^{-3}), H_2 fraction, and total photodissociation and ionization rate of H_2 (s^{-1}). The molecular clouds are coloured left to right: green, red, and orange to contrast each map.

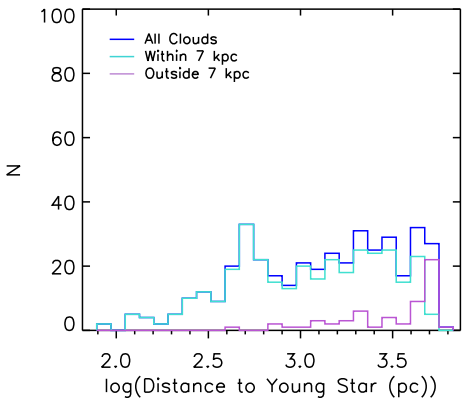

Figure 11. Histogram of the distance of the nearest young (≤10 Myr) star to a cloud boundary (pc). *N* is the total number of clouds in each bin. The clouds are separated into total cloud population (blue), inner clouds (turquoise), and outer clouds (plum) as explained in Section 4.3.

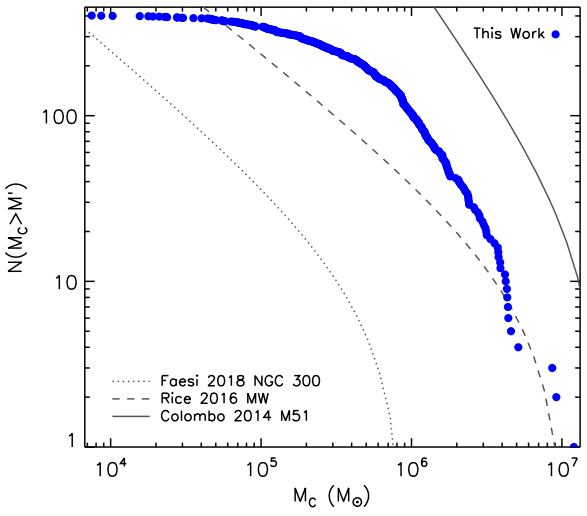

Figure 12. Cumulative function of our molecular cloud masses ($M_\odot$, blue dots), compared to functions for NGC 300 (Faesi et al. 2018) (dotted line), the Milky Way (Rice et al. 2016) (dashed line), and M51 (Colombo et al. 2014) (dash–dotted line).

of M51 is the most massive shown here. Clouds as massive as 10^8 $M_\odot$ are observed in our Galactic centre (Oka et al. 2001), but these massive clouds are missing from the surveys we show here and our own simulation. At the other end, we have fewer low-mass clouds because of our limit of at least 10 cells per cloud.

All of our clouds fall within the central 10 kpc radius of our galactic disc, and comprise 25 per cent of molecular mass in the disc. This is the same fraction given by Rice et al. (2016) for the Milky Way, but lower than the 54 per cent given by Colombo et al. (2014) for M51. This matches our findings in Table 3, where 75 per cent of H_2 in GHigh is of density 102 cm^{-3} or lower, close to our threshold in the clump finder.

Next, we seek to compare our cloud population to the Milky Way cloud catalogue compiled by Miville-Deschênes et al. (2017) from data by Dame et al. (2001). They find that the distributions of cloud properties differ between the inner and outer discs of the Milky Way, where the clouds in the outer disc have lower densities and lower masses, but a higher virial parameter. Colombo et al. (2014) further subdivided M51 into inner and outer spiral arms and inter-arms regions, but this detailed analysis goes beyond our resolution. M51's clouds have higher densities and masses in the central galaxy and the arms, while these properties are lowest in the inter-arm regions.

We show histograms in Fig. 13, with the cloud population divided into the inner disc (inside 7 kpc) and the outer disc (outside 7 kpc) where the H_2 and SFR fall off in Fig. 5. Each histogram contains 25 bins evenly spaced logarithmically. The cloud properties are as follows: mass, radius, volume density, surface density, velocity dispersion, and the virial parameter. Our clouds range from a little over 10^7 $M_\odot$ to a few 10^4 $M_\odot$, peaking at 10^6 $M_\odot$, and 10–70 pc in radius, peaking at 25 pc. We also show the volume density of H_2 in which the distribution favours lower densities of around 40 cm^{-3}, and ranges from about 40 to 400 cm^{-3}. The surface density peaks at about 400 $M_\odot$ pc^{-2} towards the more massive end and ranges from 60 to 2000 $M_\odot$ pc^{-2}. Our velocity dispersion histogram is even more peaked at 5 km s^{-1}, ranging from 1.5 to 60 km s^{-1}. Finally, we see that the virial parameter peaks at 1.25, which is slightly over virial equilibrium between internal kinetic and gravitational forces. The virial parameter is the most peaked of all our distributions. However, clouds with $\alpha_{vir} \approx 2$ are still considered to be marginally gravitationally bound (Dobbs et al. 2014).

When we consider the clouds as divided between inner and outer discs, a different story emerges from that of Miville-Deschênes et al. (2017). We see very little regional distinctions. There are fewer clouds in the outer disc, given that it also covers a smaller surface area and lower H_2 density. The mass, radius, volume, and surface density distributions are the same between the two populations. The outer clouds do not have extremes on either end, but this may be due to small-number statistics. Both inner and outer cloud distributions peak in the same locations. We do not see the drastic bi-modality as in Miville-Deschênes et al. (2017), though one explanation is that we are not able to resolve the low-density clouds that they can in their observations.

Grisdale et al. (2018) ran a similar comparison, and the values in their PPP histograms with feedback have a comparable range to ours in Fig. 13. The major difference between our simulations and theirs is that we use radiative transfer and molecular chemistry. Their histograms for mass, surface density, and volume density are more peaked, while our values are more evenly distributed throughout the range. This may be due to the fact that we have a lower star formation efficiency, and hence stars form more slowly in dense clouds, decreasing their destruction. This might lead to a greater diversity of cloud masses and densities in our simulations.

We present several relations in Fig. 14, starting with the velocity dispersion versus cloud radius, first described by Larson (1981). We compare to the relation as found by Solomon et al. (1987) for the Milky Way and Bolatto et al. (2008) for the Local Group, which are quite similar. However, modern surveys reveal high scatter in this relation. Colombo et al. (2014) find an extremely weak correlation between velocity dispersion and radius and that most of their clouds exhibit a velocity dispersion above these two fits for every sector of M51. We also see a similar distribution as in M51, and a poor fit to this relation. This is due to our non-constant surface density for the cloud population.

More recently, Heyer et al. (2009) suggest that instead of the Larson relation it is more useful to examine $\sigma_v/R_C^{0.5}$ versus Σ_C. Earlier surveys had a low spatial resolution and as a consequence mistakenly took the surface density to be constant across all clouds. Modern surveys show a range of surface densities across many galaxies (Sun et al. 2018), which we also find in Fig. 13. The top right plot in Fig. 14 shows our Heyer relation ($\sigma_v/R_C^{0.5}$ versus Σ_C) with the line of constant $\alpha_{vir} = 1$. As in Heyer et al. (2009), most of our clouds are above this line and this relation is more linear for our data than the Larson relation above. In the bottom left plot in Fig. 14, we show the virial parameter versus cloud mass. 24 per cent of our clouds have $\alpha_{vir} < 1$ and are unstable. Our average viral parameter is 2, which is in line with Rosolowsky (2007)'s findings for M31, and that they argue is not significantly different from Solomon et al. (1987)'s value for the Milky Way, 1.45.

Lastly, the bottom right plot in Fig. 14 gives the relation between cloud mass and radius. This plot is not compared to observation, however, but to another set of simulations. Fujimoto et al. (2016) in their simulations identify two separate cloud sequences that follow this relation differently, and also the same two sequences as in the Larson relation. In our simulations, however, we only find a single linear sequence. In all four plots in Fig. 14, we also differentiate inner and outer clouds, and again find no difference between the two populations.

5 DISCUSSION AND SUMMARY

RAMSES-RT (Rosdahl et al. 2013) is a moment-based radiative transfer expansion for the AMR hydrodynamics code RAMSES (Teyssier 2002). It produces, propagates, and destroys photons in distinct groups related to the ionization of hydrogen and helium, and ties these photons and species to the thermal state of the gas. Nickerson et al. (2018) presented the molecular hydrogen addition to RAMSES-RT. The most novel aspect of our H_2 model was our self-shielding implementation. Previous codes modelled self-shielding by reducing the photodissociation of H_2, whereas we modelled it by enhancing LW destruction.

In this paper, we apply our molecular chemistry model to an isolated Milky Way-like disc galaxy at three different resolutions: Glow with a minimum cell width of 97 pc, GMed at 24 pc, and GHigh at 6.1 pc. This galaxy was also used in the AGORA code comparison project (Kim et al. 2014, 2016). We use the star formation model from Rasera & Teyssier (2006), which is based on the total gas density and is independent of H_2. Furthermore, we choose not to enhance H_2 formation with a clumping factor. We seek to directly simulate the interaction of radiation and chemistry without any adjustable parameters on the galactic scale.

Just as with other simulations that maintain the SFR independent of H_2 density (Capelo et al. 2018; Lupi et al. 2018), the molecular–SFR relation observed by Bigiel et al. (2008) arises naturally. Tying H_2 to the star formation explicitly is not necessary to reproduce their relationship on the kpc scale. When considering the maximum H_2 fraction achieved, we only reach 0.985 in GHigh. This is a little lower than in other works (Gnedin & Kravtsov 2011; Christensen et al. 2012; Hu et al. 2016; Capelo et al. 2018; Lupi et al. 2018), who do find volume elements with 100 per cent H_2. These codes all use a clumping factor to account for unresolved cloud structure. However, our number is fairly close considering that we have no such factor. With sufficient resolution, a clumping factor may not be necessary.

There are several caveats to this work. We neglect magnetic fields, which play a role in molecular cloud dynamics (Crutcher

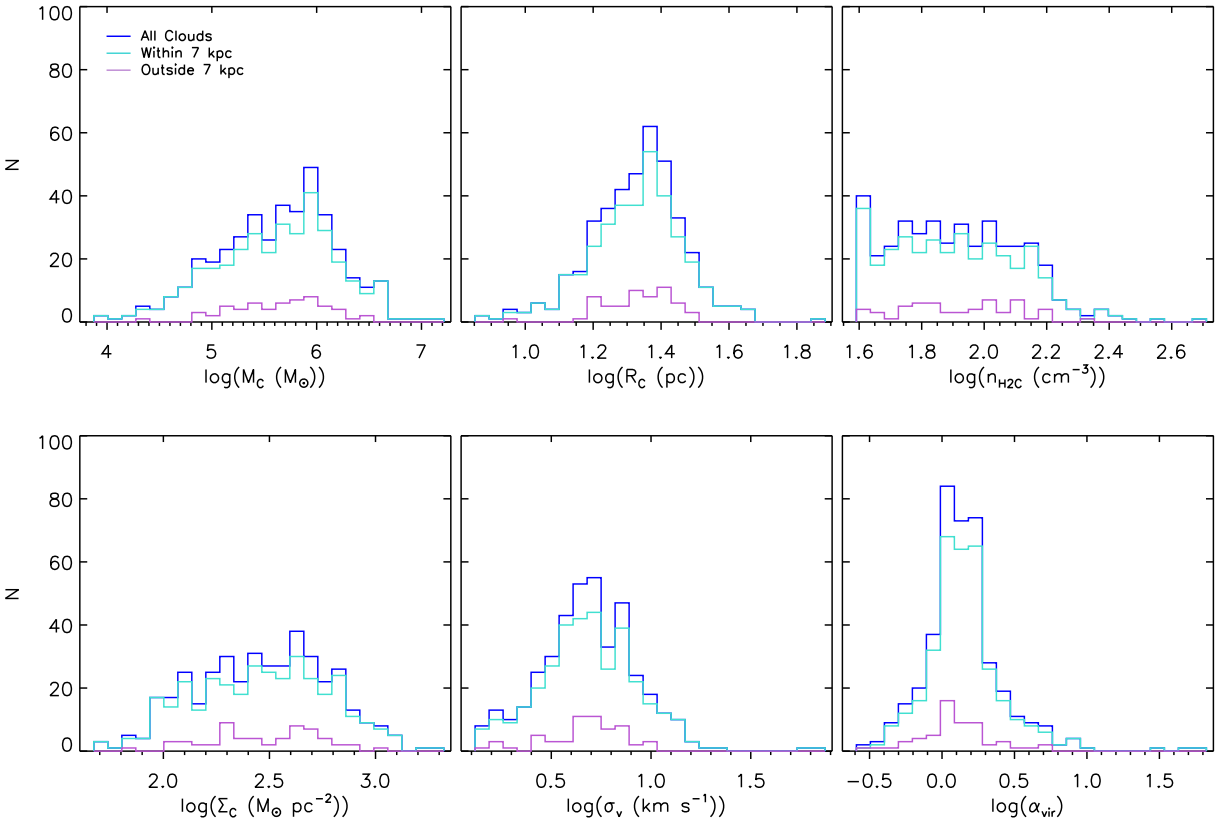

Figure 13. Histograms for our total cloud population (blue), inner (turquoise), and outer clouds (plum), left to right, top to bottom: mass ($M_\odot$), radius (pc), volume density (cm^{-3}), surface density ($M_\odot\ pc^{-2}$), velocity dispersion ($km\ s^{-1}$), and virial parameter. *N* is the total clouds in each bin.

2012), and a wider cosmological context. Inflows and outflows of gas from a galaxy can profoundly impact it. Dust, the main formation catalyst for H_2 and an important radiation shield, is not separately tracked in RAMSES-RT. Instead, we take the dust fraction of a cell to be the neutral hydrogen fraction. Stellar winds are another missing process. We are unable to resolve the Stömgren spheres of ionized gas around hot, young stars, which we can fix through post-processing. We also cannot resolve lower mass clouds properly even at our highest resolution, GHigh.

None of the three resolutions converge, and indeed, due to the differing star formation thresholds, this work cannot be a true convergence test. Instead, we present a convergence study. The phase diagrams in Fig. 7 and the molecular fraction cumulative function in Fig. 9 show that the H_2 abundance is approaching convergence between GMed and GHigh, even if it has not yet reached it.

In summary, we perform a complete analysis of the H_2 gas in Milky Way-like simulated disc galaxies from the morphology to individual molecular clouds, and find the effect resolution has on H_2 content.

Star formation history: The star formation history of the galaxies helps us determine when all three resolutions reach a semisteady equilibrium state. We choose 800 Myr as the time at which to analyse the galaxies in the subsequent sections.

Morphology: Resolution profoundly affects the structure and complexity of each galaxy. GLow is smooth and comparatively featureless aside from some spiral arms in the centre, while GMed has many more arms with clumps and GHigh not only has arms and clumps, but also intricate filamentary structure between the arms. H_2 traces the densest gas regions and remains confined to the disc, while H I is more diffuse and additionally traces the gas ejected from the disc. H_2 effectively blocks the dissociating and ionizing radiation from young stars.

Comparison to observables: We present the observable properties of molecular gas on the kpc and overall gas content scales. Overall, our molecular fraction of neutral gas is comparable to observations for GHigh and GMed, but falls short for GLow. Our surface density profiles of H_2, H I, and SFR, like their morphology, change with resolution. GLow is dominated by H I for its entirety, while GMed and GHigh host H_2-dominated central regions. GLow and GMed have central SFR spikes and GHigh has a flat SFR profile, due to morphological quenching from its central bulge. We also compare the KS relation of our galaxies to data from a large survey (Bigiel et al. 2008). Our simulations fall within their margins, for both the total neutral gas relation and the pure molecular relation. We show, as in Schruba et al. (2011), that the H_2–SFR relation is tighter than the H I–SFR relation.

Phase diagrams: These vivisect our galaxies into individual volume elements. n_H–T diagrams show that all three galaxies largely follow the same contours, but how low the temperature goes and how high the density reaches depend on resolution. This profoundly affects the phase diagrams for H_2 while the other two hydrogen species are less affected by resolution. H_2 reaches peak abundances of 0.704, 0.925, and 0.985 in the GLow, GMed, and GHigh galaxies respectively.

Molecular distribution: We quantify the percentage of molecular gas in low-density regions. For GLow, GMed, and GHigh, respectively, half of the H_2 is in cells with densities below 5.57,

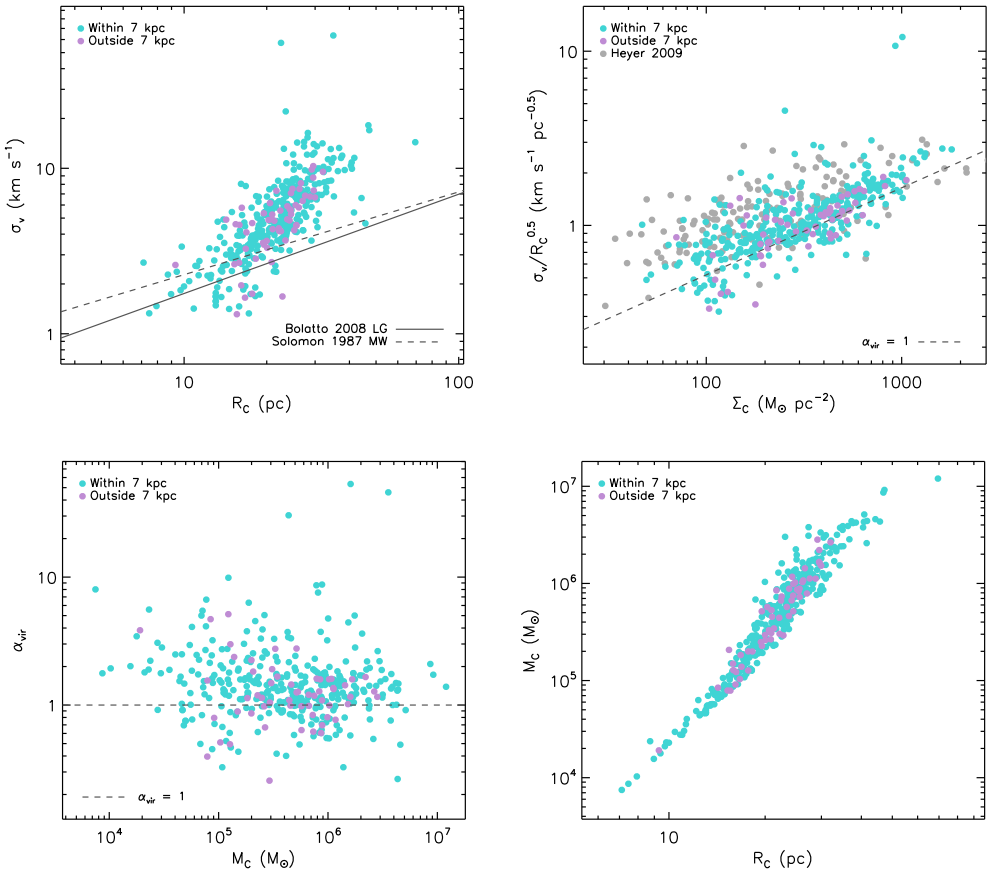

Figure 14. Relationships for our cloud populations, divided into inner clouds (turquoise) and outer clouds (plum), left to right, top to bottom: velocity dispersion (km s^{-1}) versus radius (pc) compared to observations of the Milky Way (Solomon et al. 1987) (dashed line) and the Local Groups (Bolatto et al. 2008) (dash–dotted line); velocity dispersion divided by the radius' square root (km s^{-1} pc$^{-0.5}$) versus surface density ($M_\odot$ pc^{-2}) with the line of unitary virial parameter (dashed line) compared to Milky Way data (Heyer et al. 2009); virial parameter versus cloud mass, with the line of unitary virial parameter (dashed line); and cloud mass ($M_\odot$) versus radius (pc).

12.0, and 37.8 cm^{-3} and in cells with H_2 fractions below 0.254, 0.507, and 0.570. This shows that a significant amount of H_2 gas is diffuse and mixed with H I.

Molecular clouds: We use GHigh to analyse our molecular clouds because it is the only resolution that produces gas concentrations similar to observed molecular clouds. Our molecular clouds trace the spiral arms, and the cumulative mass function is similar to that of the Milky Way. 25 per cent of H_2 is in these molecular clouds. None of the molecular clouds contain young stars. Our molecular clouds' properties (mass, radius, gas density, surface density, velocity dispersion, and the virial parameter) are similar to observations, and our average virial parameter is 2. However, when we split the histograms between the inner and outer discs, we get very similar distributions, unlike observations that show different distributions (Miville-Deschênes et al. 2017). Our clouds correspond to the Heyer et al. (2009) relation better than the Larson (1981) relation, in keeping with modern findings that molecular clouds have non-constant surface densities.

Considering the entire body of work between Nickerson et al. (2018) and this paper, we have shown that the laws that govern H_2 on the chemical scale give rise to relations that govern H_2 on the galactic scale. We have demonstrated that high resolution is critical in galaxy simulations to properly form H_2 without the need for a clumping factor.

In future, we can use our model further to explore both H_2 and H I observations. It would be interesting to see how galaxy mergers affect both species (Ellison, Catinella & Cortese 2018). On the molecular side, by adding CO to the code we can examine the relationship between H_2 and CO, the main observable of molecular gas, to further our work in Section 3.5. Our model should be tested in regimes beyond a standard Milky Way disc, such as in low-metallicity dwarf galaxies (Hu et al. 2016), or in the cold outflows from active galactic nuclei (Aalto 2015). Concerning H I, we can now study the origins of the high-velocity clouds above our own Milky Way and other galaxies (Wakker & van Woerden 1997). On even grander scales, we can compare to large-scale H I surveys such as the ALFALFA (Haynes et al. 2011) in the context of the 'too-big-to-fail problem' (Boylan-Kolchin, Bullock & Kaplinghat 2011) and results from the upcoming Square Kilometre Array (Aharonian et al. 2013). These are just a few of the many applications for RAMSES-RT with both H_2 and H I chemistry that we may explore in future.

ACKNOWLEDGEMENTS

We thank the anonymous reviewers for their insightful comments. SN was supported by the University of Zürich Candoc Scholarship, and used the Piz Daint supercomputer in the Swiss National Supercomputing Centre in Lugano. JR was funded by the ORAGE

project from the Agence Nationale de la Recherche under grant ANR-14-CE33-0016-03.

REFERENCES

Aalto S., 2015, in Daisuke I., Ken-ichi T., Alwyn W., Leonardo T., eds, ASP Conf. Ser. Vol. 499, Revolution in Astronomy with ALMA. Astron. Soc. Pac., San Francisco, p. 85
Abel T., Anninos P., Zhang Y., Norman M. L., 1997, New Astron., 2, 181
Accurso G. et al., 2017, MNRAS, 470, 4750
Aharonian F. et al., 2013, preprint (arXiv:e-print)
Baczynski C., Glover S. C., Klessen R. S., 2015, MNRAS, 454, 380
Bakes E. L. O., Tielens A. G. G. M., 1994, ApJ, 427, 822
Bergin E. A., Hartmann L. W., Raymond J. C., Ballesteros-Paredes J., 2004, ApJ, 612, 921
Bertoldi F., McKee C. F., 1992, ApJ, 395, 140
Bialy S., Bihr S., Beuther H., Henning T., Sternberg A., 2017, ApJ, 835, 126
Bigiel F., Leroy A., Walter F., Brinks E., de Blok W. J. G., Madore B., Thornley M. D., 2008, AJ, 136, 2846
Blaauw A., 1964, ARA&A, 2, 213
Black J. H., 1981, MNRAS, 197, 553
Bleuler A., Teyssier R., Carassou S., Martizzi D., 2014, Computational Astrophysics and Cosmology, 2, 1
Blitz L., Thaddeus P., 1980, ApJ, 241, 676
Bolatto A. D., Leroy A. K., Rosolowsky E., Walter F., Blitz L., 2008, ApJ, 686, 948
Bolatto A. D., Wolfire M., Leroy A. K., 2013, ARA&A, 51, 207
Boselli A., Cortese L., Boquien M., Boissier S., Catinella B., Gavazzi G., Lagos C., Saintonge A., 2014, A&A, 66, 1
Boylan-Kolchin M., Bullock J. S., Kaplinghat M., 2011, MNRAS, 415, 40
Bruzual G., Charlot S., 2003, MNRAS, 344, 1000
Burgh E., France K., McCandliss S., 2007, ApJ, 658, 446
Burton M. G., Hollenbach D. J., Tielens A. G. G. M., 1990, ApJ, 365, 620
Capelo P. R., Bovino S., Lupi A., Schleicher D. R. G., Grassi T., 2018, MNRAS, 475, 3283
Catinella B. et al., 2018, MNRAS, 476, 875
Cazaux S., Tielens A. G. G. M., 2002, ApJ, 575, L29
Cen R., 1992, ApJS, 78, 341
Chabrier G., 2003, PASP, 115, 763
Christensen C., Quinn T., Governato F., Stilp A., Shen S., Wadsley J., 2012, MNRAS, 425, 3058
Colombo D. et al., 2014, ApJ, 784
Crutcher R. M., 2012, ARA&A, 50, 29
Dame T. M., Hartmann D., Thaddeus P., 2001, ApJ, 547, 792
Dobbs C. L. et al., 2014, in Henrik B., Ralf S. K., Cornelis P. D., Thomas H., eds, Protostars and Planets VI. Univ. Arizona Press, Tucson, p. 3
Dobbs C. L., Glover S. C. O., Clark P. C., Klessen R. S., 2008, MNRAS, 389, 1097
Dove J. E., Mandy M. E., 1986, ApJ, 311, L93
Draine B. T., Bertoldi F., 1996, ApJ, 468, 269
Duarte-Cabral A., Dobbs C. L., 2016, MNRAS, 458, 3667
Dubey A., Reid L. B., Fisher R., 2008, Phys. Scr. T, T132, 1
Ellison S. L., Catinella B., Cortese L., 2018, MNRAS, 478, 3447
Faesi C. M., Lada C. J., Forbrich J., 2018, ApJ, 857, 19
Faucher-Giguère C.-A., Lidz A., Zaldarriaga M., Hernquist L., 2009, ApJ, 703, 1416
Ferland G. J., Korista K. T., Verner D. A., Ferguson J. W., Kingdon J. B., Verner E. M., 1998, PASP, 110, 761
Forrey R. C., 2013, ApJ, 773, L25
Fryxell B. et al., 2000, ApJS, 131, 273
Fujimoto Y., Bryan G. L., Tasker E. J., Habe A., Simpson C. M., 2016, MNRAS, 461, 1684
Gallagher M. J. et al., 2018, ApJ, 858, 90
Genzel R., Stutzki J., 1989, ARA&A, 27, 41
Girichidis P. et al., 2016, MNRAS, 456, 3432
Glassgold A. E., Langer W. D., 1974, ApJ, 193, 73
Glassgold A. E., Galli D., Padovani M., 2012, ApJ, 756, 157
Glover S. C., Federrath C., Low M. M., Klessen R. S., 2010, MNRAS, 404, 2
Glover S. C. O., Abel T., 2008, MNRAS, 388, 1627
Glover S. C. O., Clark P. C., 2012, MNRAS, 421, 116
Glover S. C. O., Mac Low M. M., 2007a, ApJ, 169, 239
Glover S. C. O., Mac Low M. M., 2007b, ApJ, 659, 1317
Gnedin N. Y., Abel T., 2001, New Astron., 6, 437
Gnedin N. Y., Kravtsov A. V., 2011, ApJ, 728, 88
Gnedin N. Y., Tassis K., Kravtsov A. V., 2009, ApJ, 697, 55
Gong M., Ostriker E. C., Wolfire M. G., 2017, ApJ, 843, 38
Grassi T., Bovino S., Schleicher D. R. G., Prieto J., Seifried D., Simoncini E., Gianturco F. A., 2014, MNRAS, 439, 2386
Grenier I. A., Casandjian J. M., Terrier R., 2005, Science, 307, 1292
Grisdale K., Agertz O., Renaud F., Romeo A. B., 2018, MNRAS, 479, 3167
Gry C., Boulanger F., Nehmé C., G. Pineau des Forêts Habart E., Falgarone E., 2002, A&A, 391, 675
Habart E., Boulanger F., Verstraete L., Walmsley C. M., G. Pineau des F., 2004, A&A, 414, 531
Haiman Z., Thoul A. A., Loeb A., 1996, ApJ, 464, 523
Halle A., Combes F., 2013, A&A, 559, A55
Haynes M. P. et al., 2011, AJ, 142, 170
Helfer T. T., Thornley M. D., Regan M. W., Wong T., Shieth K., Vogel S. N., Blitz L., Bock D. C., 2003, ApJS, 145, 259
Herbst E., 2001, Chem. Soc. Rev., 30, 168
Hernquist L., 1990, ApJ, 356, 359
Heyer M., Dame T. M., 2015, ARA&A, 53, 583
Heyer M., Krawczyk C., Duval J., Jackson J. M., 2009, ApJ, 699, 1092
Hollenbach D., McKee C. F., 1979, ApJS, 41, 555
Hopkins P. F., 2015, MNRAS, 450, 53
Hopkins P. F., Kereš D., Oñorbe J., Faucher-Giguère C. A., Quataert E., Murray N., Bullock J. S., 2014, MNRAS, 445, 581
Hu C.-Y., Naab T., Walch S., Glover S. C. O., Clark P. C., 2016, MNRAS, 458, 3528
Hui L., Gnedin N. Y., 1997, MNRAS, 292, 27
Indriolo N. et al., 2015, ApJ, 800, 40
Indriolo N., McCall B. J., 2012, ApJ, 745, 91
Jura M., 1974, ApJ, 191, 375
Katz H., Kimm T., Sijacki D., Haehnelt M. G., 2017, MNRAS, 468, 4831
Kennicutt R. C., 1998, ApJ, 498, 541
Kennicutt R. C., Jr, 1989, ApJ, 344, 685
Khoperskov S. A., Vasiliev E. O., 2017, MNRAS, 468, 920
Khoperskov S. A., Vasiliev E. O., Sobolev A. M., Khoperskov A. V., 2013, MNRAS, 428, 2311
Khoperskov S. A., Vasiliev E. O., Ladeyschikov D. A., Sobolev A. M., Khoperskov A. V., 2016, MNRAS, 455, 1782
Kim D. et al., 2016, ApJ, 833, 16
Kim J.-h. et al., 2014, ApJS, 210, 14
Kravtsov A. V., 1999, PhD thesis, New Mexico State University
Krumholz M. R., 2013, MNRAS, 436, 2747
Krumholz M. R., Gnedin N. Y., 2011, ApJ, 729, 36
Krumholz M. R., McKee C. F., Tumlinson J., 2008, ApJ, 689, 865
Kuhlen M., Krumholz M. R., Madau P., Smith B. D., Wise J., 2012, ApJ, 749, 36
Larson R. B., 1981, MNRAS, 194, 809
Leroy A. K. et al., 2009, AJ, 137, 4670
Leroy A. K. et al., 2013, AJ, 146, 19
Leroy A. K. et al., 2017, ApJ, 846, 71
Leroy A. K., Walter F., Brinks E., Bigiel F., de Blok W. J. G., Madore B., Thornley M. D., 2008, AJ, 136, 2782
Levermore C. D., 1984, J. Quant. Spectrosc. Radiat. Transfer, 31, 149
Lupi A., Bovino S., Capelo P. R., Volonteri M., Silk J., 2018, MNRAS, 474, 2884
Martig M., Bournaud F., Teyssier R., Dekel A., 2009, ApJ, 707, 250
Martin P. G., Keogh W. J., Mandy M. E., 1998, ApJ, 499, 793
McKee C. F., Krumholz M. R., 2010, ApJ, 709, 308
McKee C. F., Ostriker E. C., 2007, ARA&A, 45, 565
Micic M., Glover S. C., Federrath C., Klessen R. S., 2012, MNRAS, 421, 2531

Miville-Deschênes M.-A., Murray N., Lee E. J., 2017, ApJ, 834, 1
Navarro J. F., Frenk C. S., White S. D. M., 1997, ApJ, 490, 493
Nelson R. P., Langer W. D., 1997, ApJ, 482, 796
Nickerson S., Teyssier R., Rosdahl J., 2018, MNRAS, 479, 3206
Oka T., Hasegawa T., Sato F., Tsuboi M., Miyazaki A., Sugimoto M., 2001, ApJ, 562, 348
Omukai K., 2000, ApJ, 534, 809
Osterbrock D. E., Ferland G. J., 2006, Astrophysics of Gaseous Nebulae and Active Galactic Nuclei. Univ. Science Books, Sausalito, CA
Palla F., Salpeter E. E., Stahler S. W., 1983, ApJ, 271, 632
Pallottini A., Ferrara A., Bovino S., Vallini L., Gallerani S., Maiolino R., Salvadori S., 2017, MNRAS, 471, 4128
Pan H.-A., Fujimoto Y., Tasker E. J., Rosolowsky E., Colombo D., Benincasa S. M., Wadsley J., 2015, MNRAS, 453, 3082
Pelupessy F. I., Papadopoulos P. P., van der Werf P., 2006, ApJ, 645, 1024
Rasera Y., Teyssier R., 2006, A&A, 27, 1
Rice T. S., Goodman A. A., Bergin E. A., Beaumont C., Dame T. M., 2016, ApJ, 822, 52
Richings A. J., Schaye J., 2016, MNRAS, 458, 270
Richings A. J., Schaye J., Oppenheimer B. D., 2014a, MNRAS, 440, 3349
Richings A. J., Schaye J., Oppenheimer B. D., 2014b, MNRAS, 442, 2780
Robertson B. E., Kravtsov A. V., 2008, ApJ, 680, 1083
Röllig M. et al., 2007, A&A, 467, 187
Roman-Duval J., Jackson J. M., Heyer M., Rathborne J., Simon R., 2010, ApJ, 723, 492
Rosdahl J., Teyssier R., 2015, MNRAS, 449, 4380
Rosdahl J., Blaizot J., Aubert D., Stranex T., Teyssier R., 2013, MNRAS, 436, 2188
Rosdahl J., Schaye J., Teyssier R., Agertz O., 2015, MNRAS, 451, 34
Rosen A., Bergman J. N., 1995, ApJ, 440, 634
Rosolowsky E., 2005, PASP, 117, 1403
Rosolowsky E., 2007, ApJ, 654, 240
Saintonge A. et al., 2017, ApJS, 233, 22
Schmidt M., 1959, ApJ, 129, 243
Schruba A. et al., 2011, AJ, 142, 37
Smith R. J., Glover S. C. O., Clark P. C., Klessen R. S., Springel V., 2014, MNRAS, 441, 1628
Sofue Y., 2018, PASJ, 70, 106
Solomon P. M., Rivolo A. R., Barrett J., Yahil A., 1987, ApJ, 319, 730
Springel V., 2005, MNRAS, 364, 1105
Stecher T. P., Williams D. A., 1967, ApJ, 149, L29
Sternberg A., Le Petit F., Roueff E., Le Bourlot J., 2014, ApJ, 790, 10
Strömgren B., 1939, ApJ, 89, 526
Sun J. et al., 2018, ApJ, 860, 172
Tasker E. J., Tan J. C., 2009, ApJ, 700, 358
Teyssier R., 2002, A&A, 385, 337
Teyssier R., Pontzen A., Dubois Y., Read J. I., 2013, MNRAS, 429, 3068
Thompson R., Nagamine K., Jaacks J., Choi J.-H., 2014, ApJ, 780, 145
Tomassetti M., Porciani C., Romano-Diaz E., Ludlow A. D., 2014, MNRAS, 446, 3330
Verner D. A., Ferland G. J., Korista K. T., Yakovlev D. G., 1996, ApJ, 465, 487
Wadsley J. W., Stadel J., Quinn T., 2004, New Astron., 9, 137
Wadsley J. W., Keller B. W., Quinn T. R., 2017, MNRAS, 471, 2357
Wakker B. P., van Woerden H., 1997, ARA&A, 35, 217
Walter F., Brinks E., de Blok W. J. G., Bigiel F., Kennicutt R. C., Thornley M. D., Leroy A., 2008, AJ, 136, 2563
Werner M. W., Becklin E. E., Neugebauer G., Series N., Aug N., 1977, Science, 197, 723
Williams J. P., McKee C. F., 1997, ApJ, 476, 166
Wolcott-Green J., Haiman Z., Bryan G. L., 2011, MNRAS, 418, 838
Wolfire M. G., Mckee C. F., Hollenbach D., 2003, ApJ, 587, 278
Wolfire M. G., Hollenbach D., Mckee C. F., 2010, ApJ, 716, 1191
Young J. S., Scoville N. Z., 1991, ARA&A, 29, 581

This paper has been typeset from a TEX/LATEX file prepared by the author.